

Correlation Dynamics and Single-Atom Detection with Ultracold Metastable Helium

A Thesis

submitted to

Indian Institute of Science Education and Research Pune
in partial fulfillment of the requirements for the
BS-MS Dual Degree Programme

by

Rohit Patil



Indian Institute of Science Education and Research Pune
Dr. Homi Bhabha Road,
Pashan, Pune 411008, INDIA.

April, 2020

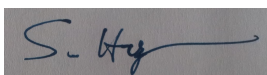
Supervisor: Dr. Sean Hodgman

© Rohit Patil 2020

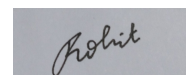
All rights reserved

Certificate

This is to certify that this dissertation entitled *Correlation Dynamics and Single-Atom Detection with Ultracold Metastable Helium* towards the partial fulfilment of the BS-MS dual degree programme at the Indian Institute of Science Education and Research, Pune represents study/work carried out by Rohit Patil, Indian Institute of Science Education and Research under the supervision of Dr. Sean Hodgman, Department of Physics, Australian National University during the academic year 2019-2020.



Dr. Sean Hodgman



Rohit Patil

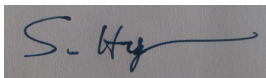
Committee:

Dr. Sean Hodgman

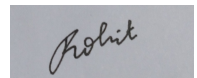
Prof. M. S. Santhanam

Declaration

I hereby declare that the matter embodied in the report entitled *Correlation Dynamics and Single-Atom Detection with Ultracold Metastable Helium* are the results of the work carried out by me at the Research School of Physics, Australian National University under the supervision of Dr. Sean Hodgman and the same has not been submitted elsewhere for any other degree.



Dr. Sean Hodgman



Rohit Patil

Acknowledgment

I want to thank my supervisor, Dr. Sean Hodgman, for his guidance and encouragement throughout the project. I would also like to thank my TAC member, Prof. M. S. Santhanam, for his support and mentorship during the years I spent at IISER Pune. I owe a special thanks to my labmate, Abbas Hussein, for helping me with the experiments and my labmates, Xianming Meng and Liangwei Wang, for working alongside me during the project. Furthermore, I owe my gratitude to the He* BEC group at the ANU, including Prof. Andrew Truscott, David Shin, Bryce Henson, Jacob Ross, Kieran Thomas and Joy Mukherjee. The group has been a constant support, brainstorming ideas and discussing problems encountered during the project. I would also like to thank Mr Colin Dedman for extending technical support with electronics.

I would also like to take this opportunity to thank Mr Jay Poria, Prof. Tim Senden and others involved in organising the FRT program, without whom this project would not have been possible. I owe my thanks to my family and friends for always being there for me. I have had a wonderful time working at the ANU and I have learnt a lot and made many cherished memories during the years I spent at IISER Pune.

Abstract

Correlation functions are a useful tool to investigate the interaction statistics in a quantum many-body system such as ultracold atoms. Historically, the study of coherence and correlations between pairs of photons in the famous Hanbury Brown and Twiss experiment was pioneering to the field of quantum optics. Since then, the area of quantum atom-optics has also gained momentum sparked by the development of lasers to cool atoms to ultra-low temperatures and the formation of Bose-Einstein condensate.

This thesis reports on progress towards an experiment to measure the second-order correlation function for a gas of ultracold metastable helium atoms. Metastable helium atoms are a unique system with single-atom detection capability that enables one to measure the correlation functions associated with the system. First, a numerical approach is taken to simulate the expected second-order correlation function for our system with given experimental parameters. The experimental sequence is then characterised and optimised to allow for the creation of a BEC. This is followed by the installation, optimisation and characterisation of the microchannel plates and delay-line detector for far-field single-atom detection and the measurement of correlation functions. This setup will form a powerful tool that can be used to perform exciting experiments with correlation functions once some minor technical issues have been resolved.

Contents

Abstract	vi
1 Ultracold atoms	2
1.1 Bose Einstein Condensation	3
1.1.1 BEC in an ideal Bose gas	3
1.1.2 BEC in a harmonic trap	5
1.2 Cooling and trapping atoms	7
1.2.1 Doppler cooling	7
1.2.2 Magneto-Optical Trap	10
1.2.3 Magnetic and optical dipole trap	12
1.3 Metastable Helium	14
1.4 Previous experiments with He*	15
2 Coherence and correlation functions	17
2.1 Coherence	17
2.1.1 Correlation function	18
2.2 1 st order correlation and interference	21
2.3 2 nd order correlation and HBT effect	24

2.4	Experimental consideration : Time of flight	27
2.5	Previous correlation experiments	30
3	Simulation of 2nd order correlations	32
3.1	Length scales in the simulation	33
3.2	Method for generating the correlated data-set	35
3.3	Calculation of the 2^{nd} order correlation function	38
3.4	Effect of finite detector resolution	40
3.5	Benchmarking the simulation	41
3.6	Results: Expected bunching in our setup	45
4	Experimental Methods and Results	47
4.1	The He* BEC Apparatus	47
4.2	Temperature estimation	49
4.2.1	Results: Absorption imaging	51
4.3	Far-field single atom detection	53
4.3.1	Microchannel plates (MCP)	54
4.3.2	Results: Time of flight signal from MCP	56
4.3.3	Delay line detector(DLD)	59
4.3.4	Data Acquisition and Processing	61
4.3.5	Results: Reconstruction of DLD signals	65
5	Conclusion	69
A	Monte-Carlo Rejection Sampling	71

Thesis Outline

The thesis is arranged as follows:

- The first two chapters cover the relevant background theory for ultracold atoms and correlation functions. Chapter 1 describes the physical principles involved in cooling and trapping atoms, it presents a few aspects of Bose-Einstein condensation and the level structure of helium.
- Chapter 2 defines correlation functions, discussing the specific cases of 1st and 2nd order correlation functions. As correlations are typically measured using time of flight method, a few experimental considerations regarding the scaling of correlations with the time of flight are discussed.
- Chapter 3 presents the numerical simulation of second-order correlation functions, which is performed to investigate the effect of experimental factors like data-binning and detector resolution on the correlation function. The procedure used to generate the 2nd order correlated dataset, method for calculating the 2nd order correlation function and the results of the simulation are discussed.
- Chapter 4 describes our experimental apparatus used for generating a BEC of He* atoms as well as the methods involved in the far-field single-atom detection and correlation measurement. Two detection schemes, namely optical detection (absorption imaging) for temperature estimation and electronic detection (with microchannel plates and delay line detector) for far-field measurement are discussed.
- Chapter 5 concludes the thesis by summarising the key outcomes achieved during the thesis. Outlook and possible future experiments are also discussed.

Chapter 1

Ultracold atoms

Ultracold atomic gases are an excellent system to investigate quantum mechanical phenomena, as cooling atoms down to temperatures close to absolute zero dramatically increases their de Broglie wavelength. Furthermore, the ability to control inter-atomic interactions either by changing the trap depth, or using an external magnetic field (Feshbach resonance) to change the scattering length makes it a good quantum simulator for probing many-body physics. For instance, one can use prototypical condensed matter systems such as the Hubbard model to simulate electrons in a solid by loading ultracold fermionic atoms like ${}^6\text{Li}$ in an optical lattice potential.

In this thesis, we use ultracold atoms to study the physics of quantum many-body systems by characterising their coherence using correlation functions. For this purpose we use standard cooling and trapping techniques to cool a gas of metastable helium (He^*) atoms to ultra-low temperatures ($\sim 10\mu\text{K}$) and obtain a Bose-Einstein condensate of He^* . We use a cold gas of He^* atoms, as it is a unique system that allows for position (and time) measurement with single-atom precision. By dropping the cold atomic cloud from a trap and measuring the 3D profile in far-field, one can obtain the momentum correlation functions associated with the atomic cloud.

1.1 Bose Einstein Condensation

The Bose-Einstein condensate (BEC) is a phase of matter which occurs at ultra-low temperatures (close to absolute zero), when a significant fraction of bosonic particles occupy the same wavefunction (usually the ground state). Satyendra Nath Bose and Albert Einstein first predicted the phenomenon of Bose-Einstein condensation during 1924-25[1]. However, it took almost 70 years for its first laboratory realisation in 1995 by the Cornell and Wieman group, who achieved a BEC for Rb atoms[2]. The development of laser cooling and trapping methods for neutral atoms during the 1980s was an essential step towards realising the first BEC. The first set of atoms to be condensed were alkali metals because of their simple electronic structure (ns^1) and the ease of access to laser cooling transition by the available lasers. The following sections present a few relevant aspects of the physics of BEC.

1.1.1 BEC in an ideal Bose gas

The uniform non-interacting Bose gas is a prototypical example of a system undergoing a phase transition to reach Bose-Einstein condensation. One can obtain the critical temperature for this transition[3], starting with the basic bosonic statistics. Using the bosonic statistics, with energy $E = \sum n_i \epsilon_i$ and number of particles $N = \sum n_i$, the grand partition function is given by,

$$\begin{aligned} Z(\beta, \mu) &= \sum_{N=0}^{\infty} \sum_k e^{-\beta(E_k - \mu N)} \\ &= \prod_i \sum_{n_i=0}^{\infty} e^{-\beta n_i (\epsilon_i - \mu)} \\ &= \prod_i \frac{1}{1 - e^{-\beta(\epsilon_i - \mu)}}. \end{aligned} \tag{1.1}$$

Using the free energy $\Omega = -k_B T \ln Z$, one obtains the following particle number distri-

bution,

$$\begin{aligned}
N &= -\frac{\partial\Omega}{\partial\mu} = \sum_i \frac{1}{e^{\beta(\epsilon_i - \mu)} - 1} = \sum_i \langle n_i \rangle \\
&= \langle n_0 \rangle + \sum_{i \neq 0} \langle n_i \rangle \\
&\equiv N_0 + N_T.
\end{aligned} \tag{1.2}$$

The average particle number in the ground state, $N_0 = 1/(e^{\beta(\epsilon_0 - \mu)} - 1)$ follows the characteristic Bose-Einstein distribution for the condensate, with the remaining particles in excited states contributing to the thermal fraction, $N_T = \sum_{i \neq 0} \langle n_i \rangle$. The critical temperature of the ideal Bose gas can be computed by applying the condition for the BEC phase transition, with $N_T = N$ where N_T is given by

$$N_T = \frac{V}{(2\pi\hbar)^3} \int \frac{4\pi p^2 dp}{e^{\beta(p^2/2m - \mu)} - 1} = \frac{V}{\lambda_T^3} \cdot g_{3/2}(e^{\beta\mu}), \tag{1.3}$$

where, $\lambda_T = \sqrt{2\pi\hbar^2/mk_B T}$ is the thermal de Broglie wavelength, and

$$g_{3/2}(z) = \frac{2}{\sqrt{\pi}} \int \frac{\sqrt{x} dx}{(z^{-1}e^x - 1)}, \tag{1.4}$$

is a special function called Bose function with $z = e^{\beta\mu}$. Setting $\mu = \epsilon_0 = 0$ and $N_T = N$ at the critical temperature T_c , one gets,

$$T_c = \frac{2\pi\hbar^2}{mk_B} \cdot \left[\frac{n}{g_{3/2}(1)} \right]^{2/3}. \tag{1.5}$$

with $g_{3/2}(1) = 2.612$. The above equation suggests that it is preferable to have a high density of light atoms like H or He to obtain a high critical temperature. Although the ideal non-interacting Bose gas is a good toy-model that shows how bosonic statistics may lead to a phase transition, ignoring interactions leads to certain artefacts such as infinite compressibility of Bose gas. These artefacts are rectified on the addition of interactions in the system.

1.1.2 BEC in a harmonic trap

We seldom study the case of uniform Bose gas during experiments, with cooling and trapping methods naturally leading to the formation of Bose-Einstein condensate in a trap. Hence, we discuss how the non-uniformity of a trap like magnetic or optical trap modifies the physics of the trapped ultracold gas compared to a uniform Bose gas (section 1.1.1). Rather than dealing with an arbitrary trap geometry, the simple case of a harmonic trap is considered (following the treatment as in [4]). It's reasonable to do so because many traps¹ close to their trap centre (minimum of the potential) can be well approximated by a harmonic trap (to the lowest order in the distance from the centre). Furthermore, close to zero temperature, the effect of two-body interactions is captured by the low energy s-wave scattering length a , with constant interaction strength $U_0 = 4\pi\hbar^2 a/m$ leading to the contact potential $U = U_0\delta(r - r')$ in position space.

Consider a condensed state of a trapped Bose gas, with all N particles occupying the same state $\phi(r)$. Using Hartree approximation, the full many-body wavefunction is given by $\Phi(r_1, \dots, r_N) = \prod_i \phi(r_i)$. The Hamiltonian of this system is,

$$H = \sum_{i=1}^N \frac{p_i^2}{2m} + V(r_i) + \sum_{j<i} U_0\delta(r_i - r_j), \quad (1.6)$$

with $V(r)$ being the external trapping potential. In terms of the wavefunction $\psi(r) = \sqrt{N}\phi(r)$ (Bogoluibov approximation), the energy functional $E = \langle \Phi | H | \Phi \rangle$ is given as,

$$E(\psi) = \int dr \frac{\hbar^2}{2m} |\nabla\psi(r)|^2 + V(r)|\psi(r)|^2 + \frac{U_0}{2} |\psi(r)|^4. \quad (1.7)$$

Minimising $E - \mu N$ with respect to ψ^* yields the ground state wavefunction (with minimum energy) given by,

$$\left(-\frac{\hbar^2}{2m} \nabla^2 + V(r) + U_0 |\psi(r)|^2 \right) \psi(r) = \mu \psi(r). \quad (1.8)$$

This is the famous *Gross-Pitaevskii equation* that describes the physics of non-uniform trapped condensates. Moreover, this equation resembles Schrödinger equation for a particle experiencing an external trapping potential $V(r)$ along with an effective potential $U_0|\psi(r)|^2$

¹like magnetic trap with bias or optical dipole trap

due to the interaction with all other particles.

For an atomic gas with a cloud size of the order $\sim R$ trapped in an isotropic harmonic potential $V(r) = \frac{1}{2}mw_0^2r^2$, potential energy for the ground state goes as $\sim mw_0^2R^2/2$ and kinetic energy scales as $\sim \hbar^2/2mR^2$. In the case of non-interacting particles in the harmonic trap, the energy is minimised at $a_{osc} \equiv R = \sqrt{\hbar/mw_0}$, which is a characteristic length scale for the oscillator. The two-body interactions can be included by adding the term $U_0|\psi(r)|^2$ from the Gross-Pitaevskii equation with the density $|\psi(r)|^2 = n(r) \sim N/R^3$.

As the number of atoms in the condensate N increases, we reach a strong coupling regime where we can ignore the kinetic energy with respect to the interaction term. Thus the radius of the interacting atomic cloud scales as $R \sim a_{osc}(Na/a_{osc})^{1/5}$ [4]. Therefore, it is justified to ignore the kinetic energy contribution for large N , which scales as $1/R^2 \sim (Na/a_{osc})^{-2/5}$ compared to potential energy scaling as $R^2 \sim (Na/a_{osc})^{2/5}$. Ignoring the kinetic energy contribution to the Gross-Pitaevskii equation is known as the *Thomas-Fermi approximation*, which yields,

$$(V(r) + U_0|\psi(r)|^2)\psi(r) = \mu\psi(r), \quad (1.9)$$

with the harmonic potential $V(r) = \frac{1}{2}m(\omega_x^2R_x^2 + \omega_y^2R_y^2 + \omega_z^2R_z^2)$ and the density $|\psi(r)|^2 = n(r)$ given by,

$$n(r) = (\mu - V(r))/U_0, \quad (1.10)$$

which has a parabolic shape due to the harmonic trapping. The boundary of the cloud is given by r such that $V(r) = \mu$, which gives the spatial extent of the cloud in the three directions known as the Thomas-Fermi radii,

$$R_i^{TF} = \sqrt{2\mu/m\omega_i^2}, \quad i = x, y, z, \quad (1.11)$$

where, the chemical potential is determined by the normalisation condition, $\int n(r)dr = N$, given by,

$$\mu = \frac{15^{2/5}}{2} \left(\frac{Na}{\bar{a}} \right)^{2/5} \hbar\bar{\omega}, \quad (1.12)$$

where, $\bar{\omega} = (\omega_x\omega_y\omega_z)^{1/3}$ and $\bar{a} = \sqrt{\hbar/m\bar{\omega}}$. Thus by fitting the Bose-Einstein condensate density profile to the Thomas-Fermi distribution and measuring the spatial extent of the atomic cloud, one can determine the number of atoms in the condensed phase (using Eq 1.11 and Eq 1.12).

1.2 Cooling and trapping atoms

To perform experiments such as measurement of correlation functions with ultracold atoms, we first need to cool and trap the gas of atoms (He^* in our case). For this purpose, we can use the light-induced forces produced by a combination of laser beams and magnetic field gradients. There are two types of light-induced forces, namely, velocity-dependent friction-like forces which slow down atoms, and position-dependent forces which spatially confine and trap the atoms. In the following sections, we briefly discuss Doppler cooling (and optical molasses) which uses a velocity-dependent force, followed by Magneto-optical trap which employs position-dependent force on top of the velocity-dependent force to cool and trap atoms (by following the treatment as in [6]). We conclude this section by discussing magnetic and optical dipole trap which play an integral role in the formation of a BEC.

1.2.1 Doppler cooling

Doppler cooling is a technique that employs a slightly off-resonant laser beam to laser cool the atoms. Firstly, consider a simple scenario of a resonant laser beam shone onto stationary atoms. When the laser beam of frequency ω_L and wave vector \mathbf{k} is incident on a stationary atom in the ground state, with a resonant (natural) frequency ω_0 , if $\omega_L = \omega_0$ there is a high probability that the atom would absorb this photon by stimulated absorption and quickly re-emit it by spontaneous emission. After absorbing the photon, the atom gains a momentum of $\mathbf{p} = \hbar\mathbf{k}$ equal to the momentum of the photon, and hence it starts moving in the initial direction of the photon. This is followed by spontaneous emission of the absorbed photon in a random direction which again imparts a momentum kick $\hbar\mathbf{k}$ causing it to gain some velocity in the direction opposite to the emitted photon. However, as the emission process is random, after multiple absorption-emission cycles, the average momentum imparted due to emission $m\langle v \rangle \rightarrow 0$. Thus effectively, the net momentum transferred to the atom can be taken to be $\hbar\mathbf{k}$ due to the absorbed photon.

The light-matter interaction, as discussed above, can be used to reduce the momentum of an atom in motion by impinging the laser light in the direction opposite to the atom's motion. However, as the atom moves, it sees the laser frequency Doppler shifted. This Doppler shift can be appropriately chosen to slow down the atoms. We now derive a quantitative expression

for the scattering force exerted by the laser beam. Consider an atom moving with a velocity \mathbf{v} , it sees the laser frequency shifted to $\omega'_L = \omega_L + \omega_D$, where $\omega_D = -\mathbf{k} \cdot \mathbf{v}$ is the Doppler shift. This causes an increase in laser frequency seen by the atoms moving into the beam. Hence to keep the laser beam resonant at the atomic transition ω_0 , the laser frequency is detuned (lowered) by the amount $\delta = \omega_L - \omega_0$ equal to the Doppler shift ω_D (Fig.1.1).

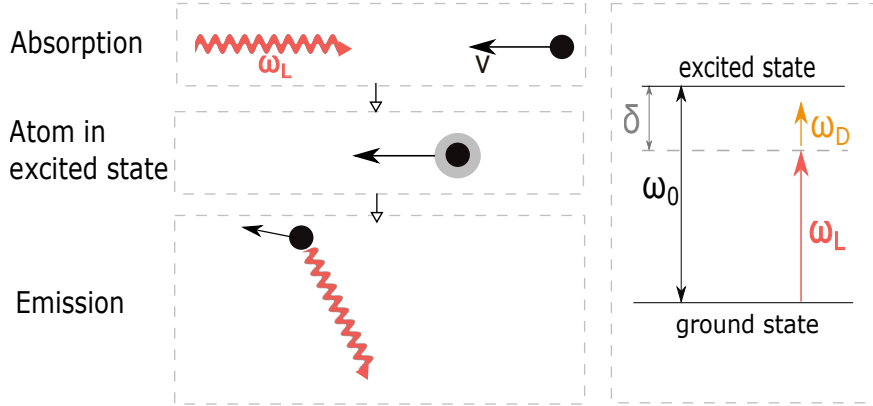


Figure 1.1: Left: A cartoon showing the steps involved in Doppler cooling for a single absorption-emission cycle. Right: An atom moving into a red-detuned beam (ω_L) sees it Doppler shifted to $\omega'_L = \omega_L + \omega_D$.

This detuning causes atoms moving into the laser beam to be shifted towards resonance and the atoms moving away from the beam to be shifted farther away from resonance. The atoms moving into the beam would absorb more photons compared to the ones moving away, thus slowing the atoms moving into the beam without much effect on the ones moving away. With each absorption-emission cycle, the atom's momentum is reduced by $p = \hbar k$. The scattering force is given by [6]

$$\mathbf{F} = \hbar \mathbf{k} \left\{ \left(\frac{\gamma}{2} \right) \frac{I/I_0}{1 + (I/I_0) + 4(\Delta/\gamma)^2} \right\}, \quad (1.13)$$

Where the quantity in the curly brackets is the scattering rate, $I_0 = \pi \hbar c / 3 \lambda^3 \tau$ is the saturation intensity, $\gamma = 1/\tau$ is the natural linewidth of the transition, $\lambda = 2\pi/k$ is the wavelength of light and $\Delta = \delta + \omega_D$. From the above expression for scattering force, one can see that large intensity ($I \gg I_0$) produces the maximum scattering force $F = \hbar k \gamma / 2$ which is just a product of momentum imparted by a photon times scattering rate $\gamma/2$. The factor of 2 comes from the fact that at high intensity the atoms are saturated to a stage where half the atoms are in the ground state and the other half in the excited state. Furthermore, note that the force scales inversely with the detuning Δ , with $\Delta = 0$ (or $\delta = -\omega_D$) giving the

maximum force for a fixed intensity.

Using only one laser beam, we can only slow down atoms moving in one direction (into the laser beam). However, we ultimately need to cool atoms moving in arbitrary directions, which can be implemented by adding an additional counter-propagating laser beam to slow atoms moving in both the directions in 1D. This scheme can be generalised to 3D by adding three pairs of counter-propagating beams along the x,y and z axes. In 1D, the net scattering force (along the direction of the motion of atom) due to the two beams, with one beam closer to resonance than others is given by

$$\begin{aligned}
 F_{net} &= F(\Delta = \delta - kv) - F(\Delta = \delta + kv) \approx -2kv \frac{\partial F}{\partial \delta} \\
 &= - \left[\left(\frac{8\hbar\delta k^2}{\gamma} \right) \frac{I/I_0}{[1 + (I/I_0) + 4(\delta/\gamma)^2]^2} \right] v \\
 &= -\alpha v,
 \end{aligned} \tag{1.14}$$

where we have assumed a small Doppler shift $kv \ll \gamma$, the above expression for scattering force causes velocity-dependent slowing (as $F \sim -\alpha v$) which resembles a frictional force. This type of Doppler cooling with counter-propagating beams is known as *optical molasses*. Furthermore, note that there is a limit to the minimum temperature achievable using Doppler cooling known as the Doppler limit. The reason for this limit is that the spontaneous emission heats the atoms. Although the average velocity imparted by emission, $\langle v \rangle \rightarrow 0$, yet the energy added to the system for multiple absorption- emission cycles don't average out to zero, that is, the average kinetic energy imparted $\frac{1}{2}m\langle v^2 \rangle$ is non-zero. The Doppler limited temperature can be found by treating the photon absorption and emission as a random walk with momentum steps of $\hbar k$. The minimum achievable temperature is given by $T_D = \hbar/2k_B\tau$ which for He* is about $40\mu K$ ($\tau \sim 98ns$ for 2^3P_2 state).

In the treatment above we had fixed the detuning δ for laser cooling, however, after a photon absorption-emission cycle, the atom would slow down, as a result, the Doppler shift kv would also be reduced. The resonance condition of $\Delta = 0$ or $\omega_0 = \omega_L + kv$ would no longer be satisfied, and this would end the slowing process. However, by using a clever technique called Zeeman slowing, one can get continued photon absorption-emission cycles even when the Doppler shift is decreasing. Zeeman slowing works by compensating for the change in

Doppler shift by adding an appropriate Zeeman shift to restore the resonance condition

$$\omega_0 + \mu B(z)/\hbar = \omega_L + kv \quad (1.15)$$

where μ is the magnetic moment associated with the transition of interest and $B(z)$ is the magnetic field along the direction of propagation of the atoms. The above condition is known as the criteria for Zeeman slowing. The desired form of a magnetic field is achieved by using an apparatus called Zeeman slower, which consists of multiple coils of gradually decreasing radii (Fig 4.1). The form of the magnetic field depends upon the velocity profile of the atoms as they traverse the Zeeman slower, which is given by $v = v_0\sqrt{1 - z/L}$ with the corresponding magnetic field $B(z) = B_0\sqrt{1 - z/L} + B_{bias}$ where v_0 and $B_0 + B_{bias}$ are the velocity and magnetic field at the beginning of the Zeeman slower, L is the length of the slower. The required length of the slower is determined by assuming that it slows down the atoms to zero velocity by the end of the slower by applying a constant scattering force, $F_{max} = \hbar k\gamma/2$. This gives $L = v_0^2/2a_{max} = mv_0^2/\hbar k\gamma$.

1.2.2 Magneto-Optical Trap

Doppler cooling, as seen in the previous section, is a velocity-dependent force like friction which slows down atoms, but it cannot confine or trap the atoms. In order to trap atoms in space, one uses an apparatus called a *magneto-optical trap* (MOT). The MOT adds a magnetic field gradient on top of the usual optical molasses (with circularly polarised beams) to generate a position-dependent force.

Similar to optical molasses, the MOT consists of 3 pairs of counter-propagating laser beams along the three directions, with each pair consisting of circularly polarised beams (σ_+ and σ_-). Furthermore, a linear magnetic field gradient is typically produced by anti-Helmholtz coils that results in the magnetic field $B(z) \sim \alpha z$, where $\alpha = dB/dz$ is the magnetic field gradient (with a linear gradient in the radial direction as well). Consider a case of a simple two-level system with angular momentum states $J = 0$ and $J = 1$. The three magnetic sublevels $M_e = -1, 0, 1$ in the excited ($J = 1$) state experience different Zeeman shifts, and hence they split in energy by different amounts at points with different magnetic fields (as shown in Fig 1.2). The electric dipole selection rules state that the transitions from $M_g = 0$ to $M_e = -1, 0, 1$ are respectively driven by σ_-, π, σ_+ polarised light beams. Hence

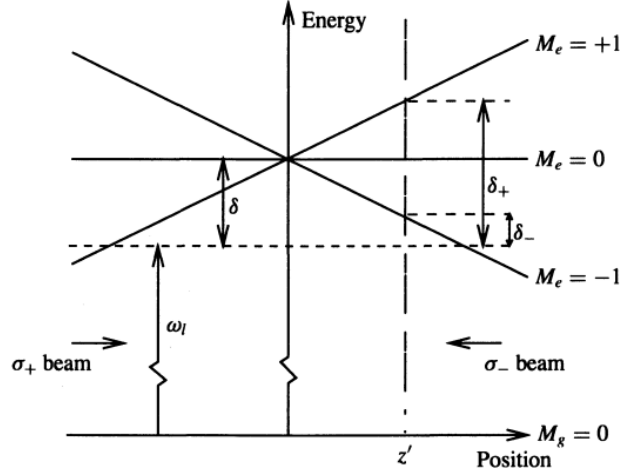


Figure 1.2: Configuration of MOT in 1D²

when in resonance, the right circularly polarised light (σ_+) would drive the transition from $M_g = 0$ to $M_e = +1$ state and similarly a left polarised light (σ_-) would drive the transition to $M_e = -1$. Both the circularly polarised beams in the MOT are red-detuned by a certain amount.

In the region $z > 0$ the sublevel $M_e = +1$ is shifted up and $M_e = -1$ is shifted down in energy by $\Delta E = g\mu_B\alpha z = \hbar\beta z$ where g is the Lande g-factor and μ_B is Bohr magneton and $\beta = g\mu_B\alpha/\hbar$. When an atom moves towards the positive z axis, it sees the beam σ_- come closer into resonance, and the beam σ_+ move away from resonance. At the point z' (Fig 1.2), the atom comes into resonance with the beam σ_- which drives the atom to $M_e = -1$ excited state by absorbing a photon, which reduces its momentum (Doppler cooling). Similarly, in the region $z < 0$, the σ_+ light would drive the atom to $M_e = +1$ state and reduce its momentum. Hence this position-dependent force disallows atoms from moving far away from the centre ($z = 0$), trapping the atoms. Similar to optical molasses, the scattering force exerted in the MOT is given by

$$\begin{aligned}
 F_{net} &= F(\Delta = \delta - kv - \beta z) - F(\Delta = \delta + kv + \beta z) \\
 &\approx -2(kv + \beta z)\frac{\partial F}{\partial \delta} \\
 &= -(\alpha v + \beta' z).
 \end{aligned} \tag{1.16}$$

²Source [6]

Notice that the scattering force in the MOT contains an extra position-dependent term $-\beta'z$ compared to the optical molasses (Eq. 1.14). Thus the atoms are both cooled and trapped by the velocity and position-dependent forces respectively. The MOT scheme, as discussed above for $J = 0 \rightarrow J = 1$ transition, also holds for any $J \rightarrow J + 1$ transition.

1.2.3 Magnetic and optical dipole trap

The cooling in the MOT ($\sim 1mK$ for our system) is insufficient to achieve a Bose-Einstein condensate (with a critical temperature of $\sim 10\mu K$ for our system). Hence further cooling to reach BEC state can be produced by evaporative cooling in an optical dipole trap (or magnetic trap). We also have an additional cooling stage prior to evaporative cooling known as in-trap cooling in the magnetic trap.

Magnetic Trap

The magnetic trap is used to confine atoms based on Zeeman effect. An atom with magnetic moment $\boldsymbol{\mu}$ placed in a magnetic field gradient \mathbf{B} would experience a force, $\mathbf{F} = -\nabla U$ with $U = -\boldsymbol{\mu} \cdot \mathbf{B}$. The magnetic field in the magnetic trap is produced by the same set of anti-Helmholtz coils used to generate the MOT with a linear magnetic gradient $B \sim \sqrt{r^2 + 4z^2}$, where z is the direction along the axis of the coils, and r is the radial direction[6]. Depending upon the sign of the magnetic moment $\boldsymbol{\mu}$ (which depends on the level M_J of the atomic state), the atom is either attracted or repelled from the origin (except $M_J = 0$ level which is unaffected by the field). Hence, only the atoms with $M_J > 0$ which are attracted towards the origin (also known as low-field seekers) are trapped by the magnetic trap with $M_J < 0$ states repelled away from the trap.

Although the trap can confine low-field seeking states, the atoms with sufficiently low energy are able to escape the trap from the trap bottom (Zero-field point). This is because the atoms with all M_J levels become degenerate at this point. Hence, the $M_J > 0$ states can spin-flip to the magnetically insensitive (or high field seeking) $M_J \leq 0$ states and fall out of the trap (This is known as Majorana spin-flip). In order to prevent the atoms from escaping the trap due to zero-field, we have an addition coil perpendicular to the anti-Helmholtz (or quadrupole coils) known as the bias coil which lifts the zero of the magnetic field (This

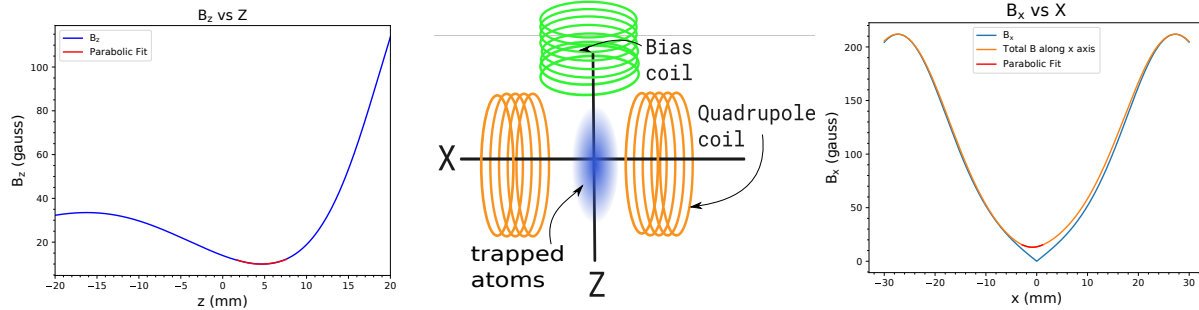


Figure 1.3: QUIC type magnetic trap (center) with the field profile along Z axis (left) and X axis (right)

magnetic field configuration is known as Quadrupole Ioffe Configuration or QUIC). The following Fig 1.3 shows the magnetic field profile along the axis of the quadrupole coils. In our setup, we also shine a 1D resonant beam on the atoms trapped in the magnetic trap to further cool the atoms by Doppler cooling (also known as in-trap cooling[22]).

Optical Dipole Trap

The optical dipole trap consists of a Gaussian beam (rather two perpendicular beams in case of crossed dipole trap as in our system) with the intensity profile

$$I(r, z) = \frac{I_0}{\sqrt{1 + (z/z_R)^2}} \exp\left(\frac{-2r^2}{w(z)^2}\right), \quad (1.17)$$

where $w(z) = w_0\sqrt{1 + (z/z_R)^2}$ is the beam waist and $z_R = \pi w_0^2/\lambda$ is the Rayleigh length. The electric field of the Gaussian beam interacts with an atom to induce a dipole moment per unit volume proportional to the field, $\mathbf{p}(\mathbf{r}) = \alpha\mathbf{E}(\mathbf{r})$, where α is the complex polarisability of the atom. Two quantities of interest while dealing with optical dipole trap are the trap potential U and dissipative scattering rate Γ given by [20]

$$\begin{aligned} U &= -\frac{1}{2}\langle\mathbf{p}(\mathbf{r}) \cdot \mathbf{E}(\mathbf{r})\rangle = -\frac{Re(\alpha)I(\mathbf{r})}{2\epsilon_0 c} \\ \Gamma &= -\frac{\langle\dot{\mathbf{p}}(\mathbf{r}) \cdot \mathbf{E}(\mathbf{r})\rangle}{\hbar\omega} = \frac{Im(\alpha)I(\mathbf{r})}{\hbar\epsilon_0 c}. \end{aligned} \quad (1.18)$$

Substituting the expression for α obtained from Lorentz oscillator model of atom[20], and using rotating wave approximation as the beam frequency ω is sufficiently close to resonance

with atomic frequency ω_0 (that is $\Delta = \omega - \omega_0 \ll \omega_0$), we find

$$\begin{aligned} U &= \frac{3\pi c^2}{2\omega_0^3} \frac{\gamma}{\Delta} I(\mathbf{r}) \\ \Gamma &= \frac{3\pi c^2}{2\omega_0^3} \left(\frac{\gamma}{\Delta}\right)^2 I(\mathbf{r}), \end{aligned} \tag{1.19}$$

where γ is the atomic damping rate due to dipole radiation. Note that the trap potential depth $U \sim I/\Delta$ and the scattering rate $\Gamma \sim -I/\Delta^2$; thus by choosing a sufficiently detuned beam (large Δ), the dissipative scattering of photons can be suppressed with respect to the dipole trap depth. In case our case we use a far detuned $1550nm$ beam for the crossed dipole trap in comparison with the He^* laser cooling transition at $1083nm$. For evaporatively cooling the atomic gas in an optical dipole trap, the trap depth U is lowered by lowering I which ‘spills’ out the highly energetic (hot) atoms for the trap and the atoms remaining in the trap re-thermalise to a lower temperature.

1.3 Metastable Helium

In our experiments, we cool and trap a gas of helium atoms in its metastable state (denoted by He^*). The first excited state of 4He is a spin-triplet, 2^3S_1 which is a metastable state (Fig 1.4), that is, it has very high lifetime of $\sim 8000s$ (with typical lifetime for other metastable noble gases being of the order $100s$ or less[7]) before decaying to the ground state. The reason being that the ground state transition, $2^3S_1 \rightarrow 1^1S_0$ is doubly forbidden by electric dipole transition (due to violation of parity rule $\Delta l = \pm 1$) and spin selection rule ($\Delta s = 0$)[8]. It can only decay slowly via a weaker mechanism of magnetic dipole transition. Thus, the metastable state effectively acts at the ground state of the system due to its long lifetime compared to the experimental time scale.

We cool and trap metastable helium atoms instead of the usual helium in the ground state because the laser cooling transition for the helium atoms ($1^1S_0 - 2^3S_1$) corresponds to a high energy of $\sim 20eV$ which is not easily accessible by the available lasers. However, the cooling transition for metastable helium ($2^3S_1 - 2^3P_2$) is readily accessible by a $1083nm$ laser. By employing the cooling principles as discussed above, the Bose-Einstein condensate of He^* was first achieved during 2001[8].

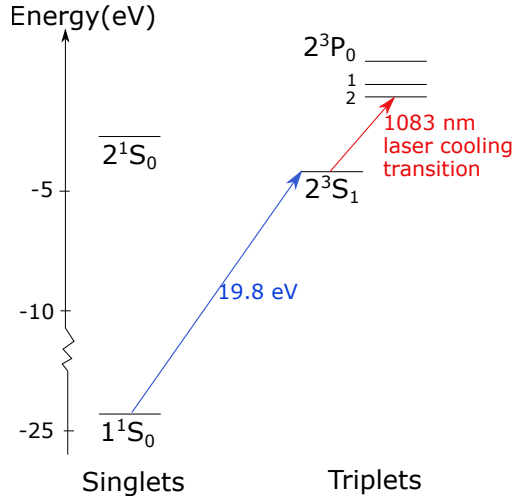
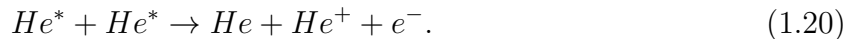


Figure 1.4: ^4He energy level diagram

The high internal energy for He^* atoms has both pros and cons. It is useful for single-atom detection, which is made possible by the liberation of its high internal energy to eject an electron from the detector surface. However, the same energy can also be liberated when the He^* atoms collide with each other, or the impurities in the chamber like water molecules, or the walls of the chamber. This leads to a major loss mechanism known as Penning ionisation, where inter-particle collisions between He^* atoms causes loss of He^* atoms via the following reaction



The atoms lost from the metastable state (He and He^+) can no longer be cooled with the laser beam resonant to the He^* cooling transition at 1083nm. Loss of metastable atoms would cause a reduction in the condensate fraction as well as trigger other collisions with He^* atoms leading to further loss of He^* atoms. The Penning ionisation is suppressed by total spin conservation in a spin polarised sample, that is, when the net spin on left hand side of Eq.1.20 becomes $S = 2$ and the net spin on the right hand side cannot exceed $S = 1$ (as $s = 0$ for He , $s = 1/2$ for both He^+ and e^-).

1.4 Previous experiments with He^*

Ultracold gas of He^* atoms among other metastable noble gases have been used to study topics like atom-optics, collisional properties, precision spectroscopic measurements and most

notably correlation measurements using atoms instead of photons.

Spectroscopic measurements such lifetime of several excited states of He (see Fig. 1.4) have been made during the past 3 decades[8], which includes the most notable measurement of the lifetime of the long-lived metastable 2^3S_1 state of He. The He* BEC group at the ANU precisely measured the lifetime of the metastable 2^3S_1 state of He to be 7870(510)s[7], which is the longest of any known excited state measured for neutral atoms. Direct measurement of the lifetime would require one to monitor the atom numbers for a sufficient fraction of the lifetime to obtain a reliable exponential fit. However, with typical trap lifetimes of a couple of seconds to minutes, it would not be very easy to get a good direct measurement of the lifetime. The He* BEC group got around this issue by indirectly measuring the XUV photon flux resulting from the decay of 2^3S_1 relative to flux for 2^3P_1 whose lifetime was previously measured by the group. This allowed them to get a precise measurement of He* lifetime, avoiding the difficulty of measuring the absolute atom numbers with time.

As BEC of He* atoms forms a coherent matter wave analogous to coherent laser beams in optics, it has been used to in atom-optics experiments such as atom interferometry experiments. The first atom-interferometry experiment with metastable Ne atoms was performed by Shimizu et al. (1992)[21]. They observed interference between Ne* atoms out-coupled from the MOT after passing through a double slit and hitting the phosphor screen after accelerating through a micro-channel plate.

The ability to locate single atoms of metastable atoms paired with delayed coincidence measurements (discussed in chap 2) have made it an ideal candidate system to measure correlation functions for atoms. T. Jelte et al(2007)[19] have performed an experiment using bosonic and fermionic He species, where they measure and compare the 2^{nd} order correlation function for both these species which show bunching and anti-bunching respectively. This experiment is an atomic variant of Hanbury Brown–Twiss experiment which highlights the role of particle exchange symmetry for 2^{nd} order coherence. Another experiment performed by Hodgman et al. (2017)[14] measures higher-order momentum correlation function (up to 3^{rd} order) for a halo of two colliding BECs of He* atoms.

Chapter 2

Coherence and correlation functions

Solving for the full many-body wave-function in quantum mechanics is difficult owing to the exponential increase in the size required to just store the information required to construct the full wave-function. The work on quantum many-body microscope[14] suggests an alternate approach to tackle the quantum many-body problem via measurement of correlation functions. The idea is that any physical observable in second quantised formalism can be expressed in terms of particle creation and annihilation operators. Thus measurement of correlation functions between these creation and annihilation operators should furnish useful information about the physical observable. For instance, the diagonal first-order correlation function between momentum space creation/annihilation operators $\langle a_p^\dagger a_p \rangle$ counts the number of the particles with momentum p . The second-order correlation function describes the two-particle interaction statistics in the system. Furthermore, the higher-order correlations give more detailed statistics of n -particle interactions in a given many-body system. Thus it is interesting to investigate the correlation functions to gain insights into the physics of quantum many-body systems.

2.1 Coherence

In classical optics, coherence describes the phase stability of light. As the phase is a function of position and time, there are two types of coherence, namely, spatial and temporal coherence. The coherence time τ_c gives the time up to which the phase of a wave remains

stable, that is, given the knowledge of the phase at some time t_1 , one can predict the phase at a later time t_2 if $|t_1 - t_2| \ll \tau_c$. For instance, a plane wave $\mathbf{E}(t) = \mathbf{E}_0 e^{-i\omega t + \phi(t)}$ with $\phi(t) = \phi_0$ has an infinite coherence time. However in a general situation one has randomly fluctuating phase occurring due to factors like spectral broadening that can reduce τ_c . Similarly, the coherence length $L_c = c\tau_c$ gives the spatial extent up to which a stable phase relationship holds between a pair of spatially separated points at a given instant of time. Coherence is a necessary condition to observe interference of light, which would be washed out by fluctuations in phase for an otherwise incoherent light.

Although the classical notion of coherence (1st order) is useful for describing interference of light which is really a single photon effect, it fails to capture the phenomenon of higher-order interference between two or more photons. The famous experiment by Hanbury Brown and Twiss performed in 1956[9] demonstrated that photons arriving from spatially separated points of a star appear bunched, which could be understood as a two-photon interference-effect. This experiment led to the redefinition of coherence to incorporate the quantum nature of light, which is summarised in the seminal paper by Glauber[15] (which also started the field of quantum optics). In the following section, we define coherence and its relation with correlation functions following the treatment of Glauber. This treatment for light can be easily generalised to massive particles like helium atoms by replacing the electric field operator for light with the corresponding bosonic/fermionic field operator for the massive particles.

2.1.1 Correlation function

The concept of optical coherence (1st order) is related to the phase stability of the light. To quantify this stability, one needs to compare the phase of light between pairs of points separated in space (or time) and check for correlations in the electric field. In general, the coherence can be quantified by specifying a sequence of correlation functions among the field strengths at n spatially (or temporally) separated points. In this section, we define correlation functions and discuss the criteria for coherence based on correlation functions.

In order to discuss correlations among electric fields at different points, consider the

following electric field operator,

$$\hat{\mathbf{E}}(\mathbf{r}, t) = \hat{\mathbf{E}}^{(+)}(\mathbf{r}, t) + \hat{\mathbf{E}}^{(-)}(\mathbf{r}, t), \quad (2.1)$$

with $\hat{\mathbf{E}}^{(+)}(\mathbf{r}, t) = \int_0^\infty \hat{\mathbf{a}}(\omega, \mathbf{r}) e^{-i\omega t} d\omega$ and $\hat{\mathbf{E}}^{(-)}(\mathbf{r}, t) = \hat{\mathbf{E}}^{(+)\dagger}(\mathbf{r}, t)$. The positive frequency part, $\hat{\mathbf{E}}^{(+)}(\mathbf{r}, t)$ acts as a photon annihilation operator[15] which reduces an n photon state $|n\rangle$ to state $|n-1\rangle$. Similarly, the negative frequency part acts as a photon creation operator.

To measure the correlation statistics among one or more photons, one performs a photo-detection experiment. A photo-detection experiment for single-photon involves absorption (or annihilation) of a photon from initial state $|i\rangle$ to go to the final state $|f\rangle = E^{(+)}(\mathbf{r}, t)|i\rangle$. The probability per unit time of occurrence of this single-photon detection event is given by

$$P_1(\mathbf{r}, t) = \sum_f |\langle f | E^{(+)}(\mathbf{r}, t) | i \rangle|^2 = \langle i | E^{(-)}(\mathbf{r}, t) E^{(+)}(\mathbf{r}, t) | i \rangle, \quad (2.2)$$

where $E^{(+)}(\mathbf{r}, t) = \hat{\mathbf{E}}^{(+)}(\mathbf{r}, t) \cdot \boldsymbol{\epsilon}$ is the component of the annihilation operator along a direction $\boldsymbol{\epsilon}$. It is easy to see from the form of $P_1 \sim \langle i | \hat{\mathbf{a}}^\dagger \hat{\mathbf{a}} | i \rangle$ that it counts the average number of photons in state $|i\rangle$, hence the rate of photo-detection, P_1 should be proportional to the number of photons in the state. Similarly, a coincidence detection of two photons, one measured at point the (\mathbf{r}, t) by acting $\hat{\mathbf{E}}^{(+)}(\mathbf{r}, t)$ followed by a second photon measured at point the (\mathbf{r}', t') by the action of $\hat{\mathbf{E}}^{(+)}(\mathbf{r}', t')$ has a rate given by

$$\begin{aligned} P_2(\mathbf{r}, t) &= \sum_f |\langle f | E^{(+)}(\mathbf{r}', t') E^{(+)}(\mathbf{r}, t) | i \rangle|^2 \\ &= \langle i | E^{(-)}(\mathbf{r}, t) E^{(-)}(\mathbf{r}', t') E^{(+)}(\mathbf{r}', t') E^{(+)}(\mathbf{r}, t) | i \rangle. \end{aligned} \quad (2.3)$$

One can notice a pattern from single and two-photon detection rates that an n -photon detection rate is a product of n pairs of field creation and annihilation operators. The n -photon coincidence rates are a special case of a more general definition of correlation functions with the n^{th} order correlation function defined as

$$G^{(n)}(\mathbf{r}_1 t_1 \dots \mathbf{r}_n t_n, \mathbf{r}_{n+1} t_{n+1} \dots \mathbf{r}_{2n} t_{2n}) = \langle E_1^{(-)} \dots E_n^{(-)} E_{n+1}^{(+)} \dots E_{2n}^{(+)} \rangle, \quad (2.4)$$

where $E_i^{(\pm)} \equiv E^{(\pm)}(\mathbf{r}_i, t_i)$ and the average $\langle * \rangle$ is also taken over the ensemble of states of the

field. The expressions for 1st and 2nd order correlation functions can be explicitly written as

$$\begin{aligned} G^{(1)}(\mathbf{r}_1 t_1, \mathbf{r}_2 t_2) &= \langle E_1^{(-)} E_2^{(+)} \rangle, \\ G^{(2)}(\mathbf{r}_1 t_1, \dots, \mathbf{r}_4 t_4) &= \langle E_1^{(-)} E_2^{(-)} E_3^{(+)} E_4^{(+)} \rangle. \end{aligned} \quad (2.5)$$

These expressions for correlation functions reduce to photon count rate and two-photon coincidence rate respectively in the special case when $\mathbf{r}_1 = \mathbf{r}_2 \equiv \mathbf{r}$ for $G^{(1)}(\mathbf{r}, \mathbf{r})$ and $\mathbf{r}_1 = \mathbf{r}_4 \equiv \mathbf{r}, \mathbf{r}_2 = \mathbf{r}_3 \equiv \mathbf{r}'$ for $G^{(2)}(\mathbf{r}, \mathbf{r}', \mathbf{r}', \mathbf{r})$ at a given time t (cf. Eq(2.2) and Eq(2.3)). In defining the correlation functions we had assumed a pure state $|i\rangle$ for the the field, however in general we have a statistical ensemble of states instead of a pure state. To account for the ensemble of field states given by density matrix $\rho = \sum_i p_i |i\rangle \langle i|$, one can replace the expectation value of a given operator $\langle \hat{\mathbf{O}} \rangle$ by $tr(\rho \hat{\mathbf{O}})$ in the density matrix formalism. Thus the expression for an n^{th} order correlation function (Eq 2.4) becomes

$$G^{(n)}(\mathbf{r}_1 t_1 \dots \mathbf{r}_n t_n, \mathbf{r}_{n+1} t_{n+1} \dots \mathbf{r}_{2n} t_{2n}) = tr(\rho E_1^{(-)} \dots E_n^{(-)} E_{n+1}^{(+)} \dots E_{2n}^{(+)}). \quad (2.6)$$

The form of $G^{(n)}$ correlation function as defined above scales with the size of the system (or photon flux) hence making it difficult to compare systems with a different number of photons. To overcome this difficulty, one normalises the correlation function with individual photon flux at each detector (\mathbf{r}, t) involved in the experiment. For instance, the 1st order normalised correlation function is written as

$$g^{(1)}(\mathbf{r}_1 t_1, \mathbf{r}_2 t_2) = \frac{G^{(1)}(\mathbf{r}_1 t_1, \mathbf{r}_2 t_2)}{\sqrt{G^{(1)}(\mathbf{r}_1 t_1, \mathbf{r}_1 t_1) \cdot G^{(1)}(\mathbf{r}_2 t_2, \mathbf{r}_2 t_2)}}. \quad (2.7)$$

Note that in the case of coincidence measurement with a single detector ($\mathbf{r}_1 = \mathbf{r}_2$ and $t_1 = t_2$) both the numerator and denominator of $g^{(1)}$ reduces to the single photon count rate $G^{(1)}(\mathbf{r}_1 t_1, \mathbf{r}_1 t_1) = \langle E_1^{(-)} E_1^{(+)} \rangle$ which scales with the photon flux, however $g^{(1)} = 1$ independent of the photon flux. The normalised n^{th} order correlation function is defined as

$$g^{(n)}(\mathbf{r}_1 t_1, \dots, \mathbf{r}_{2n} t_{2n}) = \frac{G^{(n)}(\mathbf{r}_1 t_1, \dots, \mathbf{r}_{2n} t_{2n})}{\prod_{i=1}^{2n} \sqrt{G^{(1)}(\mathbf{r}_i t_i, \mathbf{r}_i t_i)}}. \quad (2.8)$$

Although the above definition for correlation function may seem abstract or tedious at first glance, it carries a simple physical interpretation that an n^{th} order correlation function is proportional to the probability of joint detection of n photons at n spatially/temporally separated detectors, normalised to a product of individual single-photon detection probabil-

ities at the detectors. In the following section, we discuss simple examples of $g^{(1)}$ and $g^{(2)}$ correlations to highlight the role of correlation functions for quantifying coherence.

Having defined the correlation functions, we can formally state the criteria for coherence. A source of light is said to be coherent if it satisfies either of the following criteria based on a sequence of correlation functions:

1. **Fully coherent:** This requires coherence upto all order, that is

$$|g^{(n)}(\mathbf{r}_1 t_1, \dots, \mathbf{r}_{2n} t_{2n})| = 1, \quad (2.9)$$

for $n = 1, 2, \dots$

2. **N^{th} order or partially coherent:** This requires coherence upto N^{th} order given by Eq(2.9) for $n = 1, 2, \dots, N$.

The criteria, as mentioned above for coherence, allows us to differentiate sources based on coherence. For instance, a laser beam in principle is fully coherent compared to a monochromatic slice of thermal light which may be coherent only up to the 1^{st} order. Hence, one would not be able to differentiate a laser from a monochromatic section of thermal light based on the classical definition of coherence (1^{st} order) as both are at least 1^{st} order coherent and show interference pattern. Thus it is useful to analyse a sequence of correlation functions to compare coherence of various sources.

2.2 1^{st} order correlation and interference

In this section, we discuss the role of $g^{(1)}$ in a classical interference experiment[5]. In classical optics, a light beam with electric field strength $E(t)$ at a fixed point \mathbf{r} has a temporal 1^{st} order correlation function given by

$$g^{(1)}(t, t') = \frac{G^{(1)}(t, t')}{\sqrt{G^{(1)}(t, t)G^{(1)}(t', t')}} = \frac{\langle E^*(t)E(t') \rangle}{\sqrt{\langle |E(t)|^2 \rangle \langle |E(t')|^2 \rangle}}. \quad (2.10)$$

Let $t' = t + \tau$ be the time at which electric field is measured with a time delay of τ after the first measurement at t . Assuming that the light source has a constant average intensity,

that is, $\langle |E(t)|^2 \rangle = \langle |E(t')|^2 \rangle$, we have

$$g^{(1)}(\tau) \equiv g^{(1)}(t, t + \tau) = \frac{\langle E^*(t)E(t + \tau) \rangle}{\langle |E(t)|^2 \rangle}, \quad (2.11)$$

where the average $\langle * \rangle$ is taken with respect to time t (as the ensemble average of electric fields separated by τ is just a time average over t). Before discussing the interference of two beams of light, we first calculate $g^{(1)}$ for a single light beam with electric field (in the direction of polarisation) given by $E(t) = E_0 e^{-i\omega t + \phi(t)}$. Plugging this into Eq(2.11) for $g^{(1)}$, we find $g^{(1)}(\tau) = e^{-i\omega\tau} \langle e^{\phi(t+\tau) - \phi(t)} \rangle$. According to classical optics, a light wave is called coherent if it maintains a constant phase difference with time, that is, $\phi(t + \tau) - \phi(t) = k$, which leads to the condition $|g^{(1)}(\tau)| = 1$. On the other hand, if the phase oscillates randomly with time, $g^{(1)}(\tau)$ averages out to 0. Furthermore, note that the correlation function for any light source starts out at $g^{(1)}(0) = 1$ and stays $|g^{(1)}(\tau)| = 1$ if coherent, otherwise it drops to 0 for partially coherent or incoherent light.

Now consider a Michelson–Morley type interference experiment with the beam in one arm delayed by time τ with respect to the other. The electric field after interference is given as $E_{int}(t) = \{E(t) + E(t + \tau)\}/\sqrt{2}$ with average intensity $\langle I_{int}(t) \rangle \sim \langle |E_{int}(t)|^2 \rangle = \langle |E(t)|^2 + |E(t + \tau)|^2 + 2 \cdot Re\{E^*(t)E(t + \tau)\} \rangle$. Assuming constant average intensity $\langle |E(t)|^2 \rangle = \langle |E(t + \tau)|^2 \rangle$, we have

$$\begin{aligned} \langle I_{int}(t) \rangle &\sim \langle |E(t)|^2 \rangle \left(1 + Re \left\{ \frac{\langle E^*(t)E(t + \tau) \rangle}{\langle |E(t)|^2 \rangle} \right\} \right) \\ &\sim \langle |E(t)|^2 \rangle (1 + Re\{g^{(1)}(\tau)\}). \end{aligned} \quad (2.12)$$

The fringe visibility, V for interference is given by

$$V(\tau) = \frac{I_{max} - I_{min}}{I_{max} + I_{min}} = |g^{(1)}(\tau)|, \quad (2.13)$$

where we have used the fact that $I_{max} = \langle |E(t)|^2 \rangle (1 + |g^{(1)}|)$ and $I_{min} = \langle |E(t)|^2 \rangle (1 - |g^{(1)}|)$ from Eq(2.12). Qualitatively, the fringe visibility describes the contrast of the interference pattern, and it is equal to the absolute value of the 1st order correlation function. Thus a coherent light would have $V = 1$ as compared to incoherent light with 0 visibility.

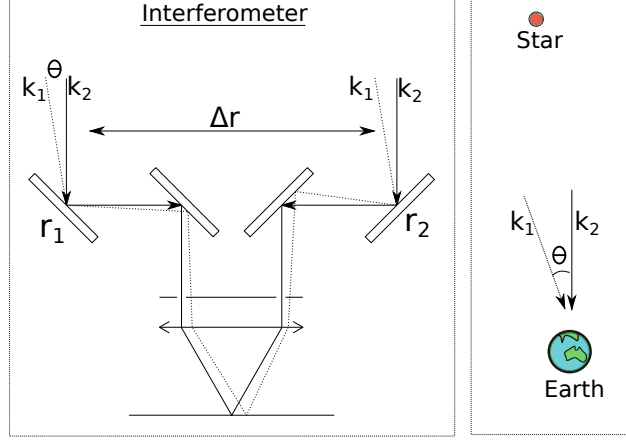


Figure 2.1: Michelson stellar interferometer: two light beams emanating from a star at an angle θ are incident on the two mirrors separated by distance Δr and interference pattern is formed on the screen ¹

Historically, a similar interferometry experiment known as Michelson stellar interferometer (Fig 2.1) has been used to measure the angular diameter $\delta\theta$ of distant bright stars². The interferometer consists of two arms with mirrors located at positions \mathbf{r}_1 and \mathbf{r}_2 separated by a distance Δr , which redirect and focus light on a screen to observe interference. In order to measure the $\delta\theta$ for a star, one can plot the spatial fringe visibility (analogous to Eq 2.13) with respect to the separation Δr to obtain $|g^{(1)}(\Delta r)|$. This gives the associated correlation length L_c (given by the width of the visibility distribution), which is related to the angular separation θ of the light source by $L_c = \lambda/\theta$. Thus by measuring the fringe visibility to obtain $|g^{(1)}(\Delta r)|$, one can determine the angular diameter of a star. For instance, consider two points on a star emitting incoherent monochromatic light beams with wave-vectors k_1 and k_2 separated by angle θ between them (Fig 2.1). The two beams enter both arms of the interferometer with electric fields $\mathbf{E}_j e^{i\mathbf{k}_j \cdot \mathbf{r}_j}$ with $j = 1, 2$ respectively, resulting in the average intensity[17]

$$\begin{aligned} \langle I(\mathbf{r}_1, \mathbf{r}_2) \rangle &\propto \langle |\mathbf{E}_1(\mathbf{r}_1) + \mathbf{E}_2(\mathbf{r}_1) + \mathbf{E}_1(\mathbf{r}_2) + \mathbf{E}_2(\mathbf{r}_2)|^2 \rangle \\ &= 4I_0 \left(1 + \cos \left(\frac{\mathbf{k}_1 + \mathbf{k}_2}{2} \cdot \Delta \mathbf{r} \right) \cos \left(\frac{k\theta \Delta r}{2} \right) \right), \end{aligned} \quad (2.14)$$

²such as Betelgeuse during 1920s

¹modified from wikimedia

where we have used the fact the beams are incoherent, that is, $\langle \mathbf{E}_i^* \cdot \mathbf{E}_j \rangle = \delta_{ij} I_0$. When the two beams arrive from the two ends of the star, $\theta = \delta\theta$ gives the angular diameter. However this method of optical interference is sensitive to fluctuations in refractive index caused by motion of the atmosphere due to the $\cos((\mathbf{k}_1 + \mathbf{k}_2) \cdot \Delta \mathbf{r}/2)$ term which rapidly fluctuates with the orientations of \mathbf{k}_1 and \mathbf{k}_2 . This reduces the fringe visibility, making it difficult to observe the interference. A solution to this problem was proposed by Hanbury Brown and Twiss, which employs intensity interferometry measuring $g^{(2)}$ instead of $g^{(1)}$ [9]. The reason being that $g^{(2)}$ relies on intensity measurements that are insensitive to atmospheric fluctuations (as discussed in the following section).

2.3 2^{nd} order correlation and HBT effect

The temporal second order correlation function $g^{(2)}(t, t')$ quantifies the correlation between intensities for two time separated points similar to $g^{(1)}(t, t')$ (Eq 2.10), which correlates the electric fields. Mathematically the 2^{nd} order correlation function can be written as[5]

$$\begin{aligned} g^{(2)}(t, t') &= \frac{G^{(2)}(t, t')}{G^{(1)}(t, t)G^{(1)}(t', t')} = \frac{\langle E^*(t)E^*(t')E(t')E(t) \rangle}{\langle |E(t)|^2 \rangle \langle |E(t')|^2 \rangle} \\ &= \frac{\langle I(t)I(t') \rangle}{\langle I(t) \rangle \langle I(t') \rangle}. \end{aligned} \quad (2.15)$$

Similarly, the 2^{nd} order spatial correlation function for beam intensities measured at a separation Δr is given by

$$g^{(2)}(\Delta r) = \frac{\langle I(r)I(r + \Delta r) \rangle}{\langle I(r) \rangle \langle I(r + \Delta r) \rangle}. \quad (2.16)$$

For a thermal source such as star which emits light with fluctuations in the intensity, $g^{(2)}$ starts with a value $g^{(2)}(0) = \langle I^2(r) \rangle / \langle I(r) \rangle^2 > 1$ and stays above 1 at least up to the coherence length L_c . For large separations $\Delta r \gg L_c$, the two intensities become uncorrelated, meaning $\langle I(r)I(r + \Delta r) \rangle = \langle I(r) \rangle \langle I(r + \Delta r) \rangle$ which gives $g^{(2)}(\Delta r) = 1$. Thus by obtaining the $g^{(2)}$ profile, one can determine L_c which in turn is related to the angular diameter of a star (as discussed in section 2.2). On the other hand, comparing this to the case of a coherent laser beam with constant intensity, we find $g^{(2)}(\Delta r) = 1$ for arbitrary separations.

As discussed in the previous section, the measurement of angular diameter of stars using

Michelson stellar interferometer suffered from atmospheric fluctuations. This led Hanbury Brown and Twiss to devise a new kind of interferometer based on the second-order correlation function. The intensity interferometry is useful because the term depending on the atmospheric fluctuations drops out, which can be seen from the second-order correlation function,

$$\begin{aligned} G^{(2)}(\mathbf{r}_1, \mathbf{r}_2) &\propto \langle I(\mathbf{r}_1)I(\mathbf{r}_2) \rangle \\ &= 4I_0^2 \left(1 + \frac{1}{2} \cos(k\theta\Delta r)\right), \end{aligned} \quad (2.17)$$

where $I(\mathbf{r}_j) = |\mathbf{E}_1(\mathbf{r}_j) + \mathbf{E}_2(\mathbf{r}_j)|^2$ is the intensity of beams on the two detectors at \mathbf{r}_1 and \mathbf{r}_2 (which replace the mirrors in the usual Michelson interferometer). For a thermal source of light such as a gas of atoms, it can be shown that [18]

$$g^{(2)}(\Delta r) = 1 + |g^{(1)}(\Delta r)|^2. \quad (2.18)$$

As $g^{(1)}(0) = 1$, the second order correlation function takes a maximum value of $g^{(2)}(0) = 2$. For $\Delta r \gg L_c$, $g^{(1)}(\Delta r) \rightarrow 0$ and $g^{(2)}(\Delta r) \rightarrow 1$. This relative enhancement of intensity correlation $g^{(2)}(\Delta r)$ for thermal light at short separations is known as the Hanbury Brown Twiss (HBT) bunching effect. The following Fig 2.2 shows a typical correlation function for light from thermal atoms and a coherent laser beam. The thermal light shows the HBT bunching effect while a coherent laser has a flat profile.

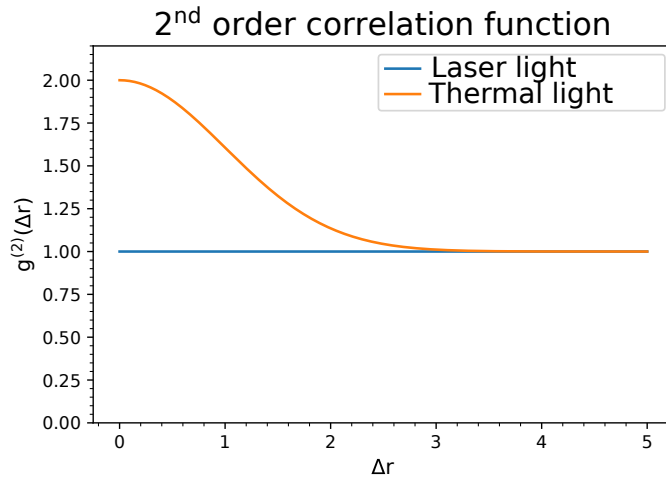


Figure 2.2: Typical 2nd order correlation function for thermal light, which shows HBT bunching with correlation length $L_c = 1$, and a laser with infinite correlation length

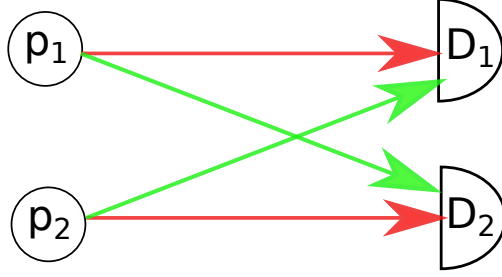


Figure 2.3: The two possible ways (Red and green) in which the particles p_1 , p_2 can be detected at the detectors D_1 and D_2 . [credit:wikimedia]

The quantum treatment of the Hanbury Brown Twiss effect, which involves treating light as photons results in an apparent conceptual difficulty regarding how two independent photons emitted from the two extremes of a star interact to register correlations at the photodetectors. This difficulty for the quantum picture of light can be resolved by considering the fact that the two emitted photons that start out as uncorrelated from the source are actually two indistinguishable bosons. This means that during the measurement process, these photons must respect the particle exchange symmetry for bosons, hence although the photons cannot interact physically, they interact via the bosonic exchange statistics which causes the correlations. Furthermore, as bosons can occupy the same state, the probability of joint detection of the two photons to lie on top of each other is enhanced, which results in the Hanbury Brown Twiss effect.

In the photon picture of light, the classical field intensity is replaced by the photon number operator $\hat{n} = \hat{a}^\dagger \hat{a}$ resulting in the following form of 2^{nd} order correlation function

$$g^{(2)}(\mathbf{r}_1, \mathbf{r}_2) = \frac{\langle \hat{n}(\mathbf{r}_1) \hat{n}(\mathbf{r}_2) \rangle}{\langle \hat{n}(\mathbf{r}_1) \rangle \langle \hat{n}(\mathbf{r}_2) \rangle}. \quad (2.19)$$

The above has a simple physical interpretation that $g^{(2)}(\mathbf{r}_1, \mathbf{r}_2)$ is related to the probability of finding a photon at \mathbf{r}_1 given a photon has been detected at \mathbf{r}_2 . Another simple way to think about the contribution of particle statistics in the $g^{(2)}$ function as suggested by Fano[10] is presented below. Consider two particles p_1, p_2 and detectors D_1, D_2 . There are 2 possible scenarios that can happen when each detector receives one particle as shown in Fig 2.3. The probability amplitude of measuring particle p_1 at the detector D_1 is written as $\langle p_1 | D_1 \rangle$. For simplicity assume that probability for detecting a particle on either of the detectors is the same, that is, $\langle p_1 | D_1 \rangle = \langle p_1 | D_2 \rangle = p_1$ and $\langle p_2 | D_1 \rangle = \langle p_2 | D_2 \rangle = p_2$.

If the two particles are distinguishable thermal bosons, the probabilities simply add up to give

$$P_d = |\langle p_1|D_1\rangle\langle p_2|D_2\rangle|^2 + |\langle p_1|D_2\rangle\langle p_2|D_1\rangle|^2 = 2|p_1|^2|p_2|^2. \quad (2.20)$$

However, if the particles are indistinguishable thermal bosons, the amplitudes first add up to give

$$P_i = |\langle p_1|D_1\rangle\langle p_2|D_2\rangle + \langle p_1|D_2\rangle\langle p_2|D_1\rangle|^2 = 4|p_1|^2|p_2|^2 = 2P_d. \quad (2.21)$$

The doubling of probability of finding indistinguishable bosons P_i relative to distinguishable ones P_d is a manifestation of the Hanbury Brown Twiss bunching. Coherent bosons as in bosons from a BEC occupy the same state and hence they are always indistinguishable, with the detection probability given by P_i . For indistinguishable fermions, the wavefunction anti-symmetry leads to

$$P_f = |\langle p_1|D_1\rangle\langle p_2|D_2\rangle - \langle p_1|D_2\rangle\langle p_2|D_1\rangle|^2 = 0. \quad (2.22)$$

The above is a manifestation of Pauli's exclusion principle. This phenomenon of reduction in joint detection probability is called anti-bunching, which is a purely quantum phenomenon.

2.4 Experimental consideration : Time of flight

In a cold atoms experiment such as ours, the objective is to measure the 2^{nd} order correlation function for a gas of cold atoms, which is released from a trap and allowed to free-fall under gravity until it hits the detector. As factors such as trapping and free fall are not present in an experiment with light, we need to understand how the time evolution of trap eigenstates is modified during free fall onto the detector. These changes in wavefunction would be reflected in the 2^{nd} order correlation function. To understand the role of these factors in the determination of correlation function, we follow the treatment of [13], which considers freely falling non-interacting particles dropped from a harmonic trap.

We start by redefining correlation functions for bosonic atoms by replacing the electric field operator in the case of light by the bosonic field operator,

$$\hat{\Psi}(\mathbf{r}) = \sum_i \phi_i(\mathbf{r})\hat{\mathbf{a}}_i, \quad (2.23)$$

where $\hat{\mathbf{a}}_i$ is the usual annihilation operator that annihilates a particle in the eigenstate $\phi_i(\mathbf{r})$ and $\hat{\Psi}(\mathbf{r})$ annihilates a particle at point \mathbf{r} . Thus the correlation functions (Eq (2.5)) after replacement with $\hat{\Psi}(\mathbf{r})$ become

$$\begin{aligned} G^{(1)}(\mathbf{r}_1, \mathbf{r}_2) &= \langle \hat{\Psi}^\dagger(\mathbf{r}_1) \hat{\Psi}(\mathbf{r}_2) \rangle, \\ G^{(2)}(\mathbf{r}_1, \mathbf{r}_2) &= \langle \hat{\Psi}^\dagger(\mathbf{r}_1) \hat{\Psi}(\mathbf{r}_1) \hat{\Psi}^\dagger(\mathbf{r}_2) \hat{\Psi}(\mathbf{r}_2) \rangle. \end{aligned} \quad (2.24)$$

The single particle density is given by $\rho(\mathbf{r}) = G^{(1)}(\mathbf{r}, \mathbf{r})$. For bosonic atoms at a particular temperature T , the 2^{nd} order correlation function factorises in terms of 1^{st} order correlation function

$$\begin{aligned} G^{(2)}(\mathbf{r}_1, \mathbf{r}_2) &= \sum_{ijkl} \phi_i^*(\mathbf{r}_1) \phi_j(\mathbf{r}_1) \phi_k^*(\mathbf{r}_2) \phi_l(\mathbf{r}_2) \langle \hat{\mathbf{a}}_i^\dagger \hat{\mathbf{a}}_j \hat{\mathbf{a}}_k^\dagger \hat{\mathbf{a}}_l \rangle \\ &= \sum_{ijkl} \phi_i^*(\mathbf{r}_1) \phi_j(\mathbf{r}_1) \phi_k^*(\mathbf{r}_2) \phi_l(\mathbf{r}_2) (\langle \hat{\mathbf{a}}_i^\dagger \hat{\mathbf{a}}_k^\dagger \hat{\mathbf{a}}_j \hat{\mathbf{a}}_l \rangle + \langle \hat{\mathbf{a}}_i^\dagger \hat{\mathbf{a}}_l \rangle \delta_{jk}) \\ &= \rho(\mathbf{r}_1) \rho(\mathbf{r}_2) + |G^{(1)}(\mathbf{r}_1, \mathbf{r}_2)|^2. \end{aligned} \quad (2.25)$$

using the Wick's theorem for factorisation of Gaussian expectations[13]. While writing the final expression for Eq 2.25, we have ignored the term $\langle \hat{\mathbf{a}}_i^\dagger \hat{\mathbf{a}}_l \rangle \delta_{jk}$ which is linear in density, with the terms retained being quadratic in density. Note that the Wick's factorisation scheme only works when T is well above the critical temperature. When close to (or below) the critical temperature for Bose-Einstein condensation, the condensate density $\rho_0(\mathbf{r})$ needs to be taken into account, which can be incorporated by adding the result for condensate density[13] to give,

$$G^{(2)}(\mathbf{r}_1, \mathbf{r}_2) = \rho(\mathbf{r}_1) \rho(\mathbf{r}_2) - \rho_0(\mathbf{r}_1) \rho_0(\mathbf{r}_2) + |G^{(1)}(\mathbf{r}_1, \mathbf{r}_2)|^2. \quad (2.26)$$

The correlation functions in Eq(2.25, 2.26) can be normalised (dividing by $\rho(\mathbf{r}_1) \rho(\mathbf{r}_2)$) to obtain $g^{(2)}(\mathbf{r}_1, \mathbf{r}_2)$. The $g^{(2)}$ function for a thermal cloud above the critical temperature (Eq 2.25, which is same as Eq2.18) starts at $g^{(2)}(\mathbf{r}, \mathbf{r}) = 2$ and decays to 1 as $|\mathbf{r}_1 - \mathbf{r}_2| \rightarrow \infty$. This is the Hanbury Brown Twiss bunching effect. Comparing this to the condensate (Eq 2.26), where for $T \rightarrow 0$ condensate state is fully occupied, which leads to cancellation of the first 2 terms, and we find $g^{(2)}(\mathbf{r}_1, \mathbf{r}_2) = 1$ for all $\mathbf{r}_1, \mathbf{r}_2$ (which is similar to the flat $g^{(2)}$ profile for laser in Fig 2.2, as BEC is an atomic analogue of a coherent laser).

In a general time of flight experiment such as ours, we assume that position space cor-

relation in far-field maps to the momentum space correlation length in a trap (cf section 3.1). This is an approximation that holds for a thermal cloud of atoms where the condensate density ρ_0 can be ignored[13].

Consider atoms in a 3D harmonic trap with frequencies ω_α , $\alpha = x, y, z$. The atoms occupy the harmonic oscillator eigenfunctions. Using the bosonic field operator $\hat{\Psi}(\mathbf{r})$ with the harmonic oscillator wavefunction, one can find the particle density $\rho(\mathbf{r}) = G^{(1)}(\mathbf{r}, \mathbf{r})$ and the 1st order correlation function

$$G^{(1)}(\mathbf{r}, \mathbf{r}') = \langle \hat{\Psi}^\dagger(\mathbf{r}) \hat{\Psi}(\mathbf{r}') \rangle = \sum_{\mathbf{m}=(m_x, m_y, m_z)} \phi_{\mathbf{m}}^*(\mathbf{r}) \phi_{\mathbf{m}}(\mathbf{r}') \frac{1}{e^{\beta(\tilde{\epsilon}_{\mathbf{m}} - \mu N)} - 1}, \quad (2.27)$$

where $\tilde{\epsilon}_{\mathbf{m}}$ is the harmonic oscillator energy without the zero point contribution $3\hbar\omega/2$ and μ is the chemical potential. In the high-temperature limit (with temperature above critical temperature and $\mu \rightarrow -\infty$), one recovers the thermal correlation function with the familiar Maxwell-Boltzmann density distribution

$$G^{(1)}(\mathbf{r}, \mathbf{r}') = \frac{N}{\lambda^3} \prod_{\alpha} \tau_{\alpha} e^{-\frac{\tau_{\alpha}}{2} \left(\frac{r_{\alpha} + r'_{\alpha}}{2\sigma_{\alpha}} \right)^2} e^{-\pi \left(\frac{r_{\alpha} - r'_{\alpha}}{\lambda} \right)^2} \quad (2.28)$$

$$\rho(\mathbf{r}) = \frac{N}{\lambda^3} \prod_{\alpha} \tau_{\alpha} e^{-\frac{\tau_{\alpha} r_{\alpha}^2}{2\sigma_{\alpha}^2}},$$

where $\tau_{\alpha} = \hbar\omega/k_B T$ and $\lambda = \hbar\sqrt{2\pi/mk_B T}$ is the de Broglie wavelength, with the in-trap correlation length given by $l^{(i)} = \lambda/\sqrt{\pi}$.

The expression for the correlation function (Eq 2.28) is only valid for atoms in a trap. In order to describe the correlations for atoms released from the harmonic trap under gravity, falling onto the detector, one needs to propagate the in-trap harmonic oscillator wavefunction to the detector surface by using the appropriate Green's function. Skipping over the tedious mathematical steps[13], one arrives at a rather simple result that the expression for wavefunction remains the same modulo phase factors and expansion factor of the form $\sqrt{1 + \omega_{\alpha}^2 t^2}$ with the following re-scaling of coordinates,

$$(x, y, z) \rightarrow \left(\tilde{x} = \frac{x}{\sqrt{1 + \omega_x^2 t^2}}, \tilde{y} = \frac{y}{\sqrt{1 + \omega_y^2 t^2}}, \tilde{z} = \frac{H - \frac{1}{2}gt^2}{\sqrt{1 + \omega_z^2 t^2}} \right), \quad (2.29)$$

where H is the location of the detector plane along the z-axis and time is measured from

trap switch off time ($t = 0$). For detection in the far field ($\omega_\alpha t \gg 1$), assuming that the drop velocity is much larger than the spread in velocities in the atomic cloud ($gt \gg \sqrt{k_B T / m \omega_\alpha^2}$), the vertical co-ordinate $\tilde{z} \approx g(t_0 - t) / \omega_z$ scales linearly with time.

The 2nd order correlation function at the time of flight (TOF) detection is given by

$$G^{(2)}(\tilde{\mathbf{r}}_1, t_1; \tilde{\mathbf{r}}_2, t_2) = \left(\frac{v(t_1)v(t_2)}{\prod_\alpha \sqrt{(1 + \omega_\alpha^2 t_1^2)(1 + \omega_\alpha^2 t_2^2)}} \right) G^{(2)}(\tilde{\mathbf{r}}_1, \tilde{\mathbf{r}}_2), \quad (2.30)$$

$$v(t) = \frac{1}{t} \left(H + \frac{1}{2}gt^2 - \frac{H - gt^2/2}{1 + \omega_z^2 t^2} \right).$$

with the atomic flux velocity $v(t)$. Comparing the expression for the in-trap 2nd order correlation function (Eq. 2.26) with the expression after the TOF measurement (Eq. 2.30), we see that the latter is just a re-scaled version of the in-trap correlation function. Luckily we don't have to worry about the expansion pre-factors which drop out on normalisation while calculating $g^{(2)}$, which is expressible as a ratio of $G^{(2)}$ s (Eq 3.12). Moreover, for harmonic potential the correlation lengths at the detector, $l^{(d)}$ increase linearly with the flight time t given by $l^{(d)} = l\sqrt{1 + \omega_\alpha^2 t^2} \approx l\omega_\alpha t$, with the in-trap correlation length l . The detector resolution also has an effect on the observed correlation functions which is discussed in section 3.4.

2.5 Previous correlation experiments

One of the first correlation experiments, as performed by Hanbury Brown and Twiss[9] in 1956 was a pioneering experiment in the field of quantum optics. Although the first correlation experiment was performed with light, the development of atom-optics have lead to similar correlation experiments with atoms instead of photons. The first atomic correlation experiment to measure the Hanbury Brown and Twiss bunching effect was performed by Yasuda and Shimizu (1996)[11] where they used a thermal gas of metastable Ne atoms.

Furthermore, the realisation of Bose-Einstein condensation allowed one to measure the correlations in a coherent matter wave made out of BEC, compared to its optical analogue of coherent laser which has a flat $g^{(2)}$ profile ($g^{(2)}(\tau) = 1$). The experiment by Schellekens et al.[12] (2005) used ultracold He* atoms to demonstrate bunching in thermal atoms and flat $g^{(2)}$ profile for a BEC of He* atoms. For the correlation measurement they dropped a cloud

of thermal and Bose-condensed atomic gas respectively from a magnetic trap onto a delay line detector (preceded by a micro-channel plate), our experiment also consists of a similar detection scheme (section 4.3).

A useful feature of performing correlation measurements with atoms compared to photons is that atoms can be either fermionic or bosonic as compared to photons which are bosons. Hence, atomic correlations allows investigation of particle statistics based on symmetry (or anti-symmetry) of wavefunction, which is not possible with photons. An experiment performed by Jelten et al [19](2007) used both bosonic and fermionic species of helium (4He and 3He respectively) and measured the corresponding 2^{nd} order correlation functions. They found the usual bunching effect for thermal bosons, however they observed a dip in $g^{(2)}(0)$ for fermions (known as anti-bunching) due to Pauli's exclusion principle (cf Eq 2.22).

As discussed above, typical correlation experiments performed measured 2^{nd} order correlation function. However, measurement of higher order correlations provides a more detailed statistics of the many-body interactions as compared to 2^{nd} order correlation function. An experiment performed by Hodgman et al.[14](2017) characterises higher order correlation functions (3^{rd} order and higher) for a system of two colliding BECs. For this particular system, they were able to characterise the higher order correlations as the functions factorise into product of 2-operator expectation values (normal density $\langle \hat{\mathbf{a}}_{\mathbf{p}}^\dagger \hat{\mathbf{a}}_{\mathbf{p}} \rangle$ and anomalous density $\langle \hat{\mathbf{a}}_{\mathbf{p}} \hat{\mathbf{a}}_{-\mathbf{p}} \rangle$) by using Wick's theorem. The experimental result for $g^{(3)}$ also verifies that higher order correlation functions contain information about the lower order functions by showing that $g^{(3)} \rightarrow g^{(2)}$ in some limit.

Chapter 3

Simulation of 2nd order correlations

In this chapter, we discuss a simple model to simulate the 2^{nd} order correlation function for a gas of thermal bosonic atoms. The objective of the simulation is to generate a sample of 2^{nd} order correlated particles with given system parameters such as temperature, trap frequencies and detector resolution.

As discussed in the section 2.3, a gas of bosonic atoms like 4He above the critical temperature for condensation exhibits an enhanced probability for joint detection close to zero separation, that is, it's second-order correlation function is bunched (also known as the Hanbury Brown Twiss bunching effect). To check whether we can observe the bunching effect on dropping a thermal cloud of He^* atoms from a trap on to the detector, we simulate the $g^{(2)}$ correlation function for these thermal atoms of He^* with the given system parameters.

We first generate a correlated data-set of multiple correlated pairs of atoms with the desired $g^{(2)}$ function, that is, a bunched profile with $g^{(2)}(\Delta z = 0) = 2$ for the thermal cloud of atoms with our system parameters. This data-set is then fed as an input to our correlator, which calculates the $g^{(2)}$ correlation function.

Possible approaches

An accurate (brute force) method to generate a correlated data-set would be to first identify the functional form of the full many-body wavefunction for the particles, followed by

sampling from the many-body probability distribution corresponding to the wavefunction. However, a problem with this approach is that it is difficult to solve for the full many-body wavefunction. Even if one succeeds in finding the high dimensional wavefunction ($3N$ dimensional for N particles), it would still be difficult to efficiently sample from the arbitrary joint probability distribution resulting from the many-body wavefunction. Furthermore, to add to the difficulties, random sampling methods such as Monte-Carlo simulation performs poorly with an increase in dimensions of the distribution, that is, one would need to sample more points in higher dimensions to represent the distribution accurately.

As the above method for generating the appropriately correlated sample of particles is infeasible, we attempted implementing an alternate method that doesn't require the knowledge of the full many-body wavefunction. In this scheme, we work backwards and first try to work out the probability distribution that would give the required 2^{nd} order correlation function. The idea is to incorporate the required correlations by sequentially sampling particles based on the distribution of initial particles. In other words, with an existing n particle distribution the $n + 1^{th}$ particle is sampled from a modified single-particle distribution with an enhanced probability of joint detection close to the previous n particles. By appropriately choosing the enhancement in probability, one can get the required correlation function. We attempted a simulation with this scheme; however, we failed to reproduce the required correlation distribution as the consecutive particles in the distribution kept clustering on top of the previous particles (details in section 3.2).

Thus we decided to simplify the scheme even further to sample a pair of particles at a time with the required correlation function. Although this method can only generate disjoint/independent pair of 2^{nd} order correlated particles, it is still able to reasonably reproduce the required correlation function as observed in an experiment (section 3.5).

3.1 Length scales in the simulation

To run the simulation for generating the two-particle correlated data-set, we work in the units of thermal length (or the size of the atomic cloud). In order to do so, we find the expressions for the two relevant length scales, namely, the thermal and correlation lengths of the atomic cloud both in-trap ($s_\alpha^{(t)}, l_\alpha^{(t)}$) and just before hitting the detector ($s_\alpha^{(d)}, l_\alpha^{(d)}$) respectively.

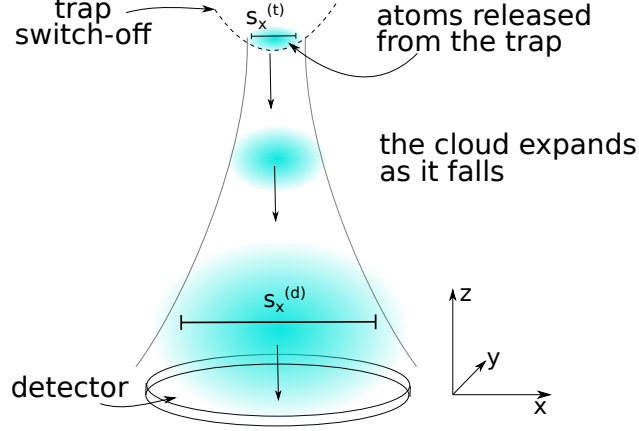


Figure 3.1: The setup of the experiment. The atomic cloud released from the trap expands and falls towards the detector, which records the positions of the individual atoms.

Consider a trap which can be approximated by a harmonic potential with trapping frequencies ω_α ($\alpha = x, y, z$) along the three axes. As the cloud is at an equilibrium temperature T we have, $\frac{1}{2}m\omega_\alpha^2 s_\alpha^2 = \frac{1}{2}k_B T$. This gives the in-trap size of the cloud in the direction α as

$$s_\alpha^{(t)} = \sqrt{k_B T / m \omega_\alpha^2}. \quad (3.1)$$

In an experiment (that we are trying to model, Fig 3.1), we switch-off the trap and let the atoms free fall towards the detector (which is positioned about 40cm below the trap). While the atoms fall towards the detector, we measure their time of flight (TOF) profile, that is, we record their positions as they hit the detector. After falling for a sufficiently long time (t_{TOF}), that is, in the far field ($\omega_\alpha t_{TOF} \gg 1$), the atomic cloud expands by a factor of $\sqrt{1 + \omega_\alpha^2 t_{TOF}^2} \approx \omega_\alpha t_{TOF}$ (see section 2.4 for details). Hence, the size of the cloud at the detector is given by $s_\alpha^{(d)} = s_\alpha^{(t)} \omega_\alpha t_{TOF}$, that is,

$$s_\alpha^{(d)} = \sqrt{\frac{k_B T}{m}} t_{TOF}. \quad (3.2)$$

In the far field, the spatial distribution of the particles maps to the initial in-trap momentum distribution, with the momentum correlation length $p_\alpha = \hbar / s_\alpha^{(t)}$ being mapped to the spatial correlation length at the detector[13],

$$l_\alpha^{(d)} = \left(\frac{p_\alpha}{m} \right) t_{TOF} = \frac{\hbar t_{TOF}}{m s_\alpha^{(t)}} = \hbar \sqrt{\frac{1}{m k_B T}} \omega_\alpha t_{TOF}. \quad (3.3)$$

Note that the correlation length $l_\alpha^{(d)}$ is proportional to the de Broglie wavelength, $\lambda = \hbar\sqrt{2\pi/mk_B T}$. This gives a simple physical picture that the de Broglie wavelength, which is a measure of length-scale for wave-function overlap is related to the correlation length. In units of the thermal length, the dimensionless correlation length is given by,

$$\tilde{l}_\alpha^{(d)} = \frac{l_\alpha^{(d)}}{s_\alpha^{(d)}} = \frac{\hbar\omega_\alpha}{k_B T}. \quad (3.4)$$

3.2 Method for generating the correlated data-set

The objective of this simulation is to sample pairs of particles which follow the correlation function for thermal bosons (similar to the thermal light in Fig 2.2), that is,

$$g^{(2)}(\Delta x, \Delta y, \Delta z) = 1 + \exp\left(-\frac{\Delta x^2}{l_x^2} - \frac{\Delta y^2}{l_y^2} - \frac{\Delta z^2}{l_z^2}\right), \quad (3.5)$$

with the pair separations $\Delta x, \Delta y, \Delta z$ and correlation lengths l_x, l_y, l_z . The data-set is generated by sampling multiple pairs of second order correlated particles using the following scheme:

1. The first particle in a correlated pair is sampled from a thermal distribution (Boltzmann distribution) with mean position=0 and spread in position (standard deviation or source size) given by the thermal length,

$$s_\alpha = \sqrt{\frac{k_B T}{m_{He}}} \cdot t_{TOF}, \quad (\alpha = x, y, z). \quad (3.6)$$

where k_B is the Boltzmann constant, T is the temperature of the atomic gas cloud, m_{He} is the mass of helium atom and t_{TOF} is the time of flight from the trap to the delay line detector. The explicit sampling distribution is given by,

$$P_1(x, y, z) \approx \exp\left(-\frac{x^2 + y^2 + z^2}{2s_\alpha^2}\right). \quad (3.7)$$

After sampling this particle, suppose that it lands at the position (x_1, y_1, z_1) . The left plot of Fig 3.2 shows an example of sampling the first particle(x_1) for a 1D section through the distribution.

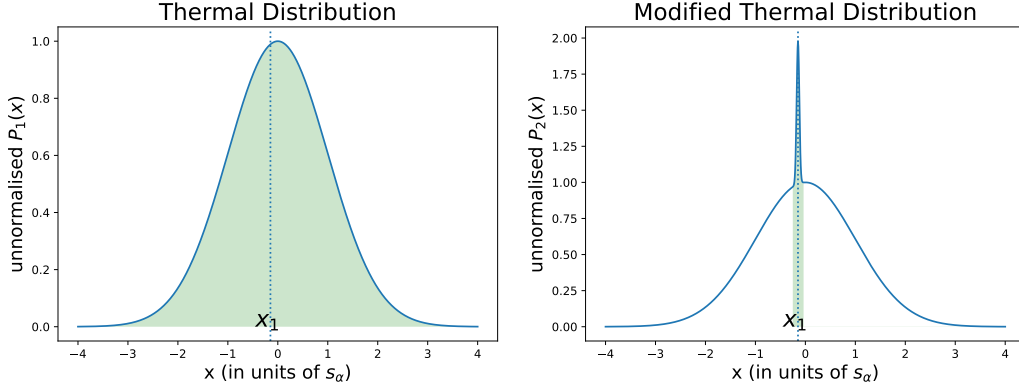


Figure 3.2: The 1st particle is sampled from the thermal distribution (left) and say it lands at x_1 . The 2nd particle is sampled from the modified distribution (right) with enhanced probability of landing close to x_1 . The green region shows the range of sampling.

2. The second particle in the pair is sampled from a modified thermal distribution which has an enhanced probability of joint detection close to the position of the first particle. This is done by adding a Gaussian distribution with spread of the correlation length onto the original thermal distribution (see Fig 3.2 right plot). The distribution for sampling the second particle thus becomes,

$$P_2(x, y, z) \approx \exp\left(-\frac{x^2 + y^2 + z^2}{2s_\alpha^2}\right) + f \cdot \exp\left(-\frac{(x - x_1)^2}{l_x^2} - \frac{(y - y_1)^2}{l_y^2} - \frac{(z - z_1)^2}{l_z^2}\right), \quad (3.8)$$

where $f = \exp\left(-\frac{x_1^2 + y_1^2 + z_1^2}{2s_\alpha^2}\right)$ is the constant pre-factor of the correlation Gaussian term which re-scales the amplitude so that we have double the joint detection probability of finding the second particle close to the first one (the bunching factor for thermal bosons with $g^{(2)}(\Delta r = 0) = 2$). This condition can be explicitly written as,

$$P_2(x_1, y_1, z_1) = 2 \cdot P_1(x_1, y_1, z_1). \quad (3.9)$$

In order to sample from the P_2 distribution, Monte-Carlo rejection sampling was used (see Appendix A). The right trace in Fig 3.2 gives an example of sampling distribution for the second particle. Note that we sample from the truncated distribution, that is, the green shaded region cutoff at the length of about a bin width+3·resolution¹ away from the first particle and not the full distribution, to reduce the time required to

¹see section 3.4 for details

generate correlated pairs in 3D. If we were to sample from the full distribution, the second particle would be sampled in larger region of space, hence reducing the chance of it contributing to the correlations for the full 3D sampling.

3. Having successfully sampled a correlated pair, we also need to generate a corresponding uncorrelated pair which would be used to normalise the second order correlation function ($G^{(2)}(\Delta z)$). For this purpose, we repeat the same steps (1 and 2) for generating a correlated pair, but instead of using a modified thermal distribution for sampling the second particle we again use the thermal distribution (Fig 3.3)

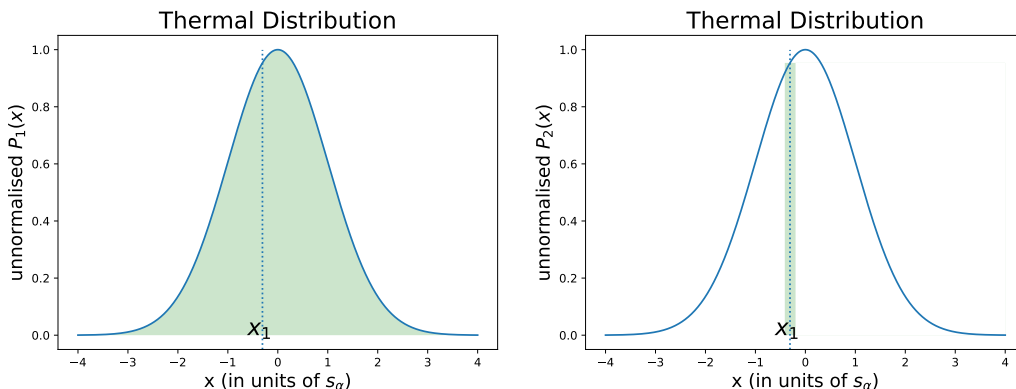


Figure 3.3: Both the 1st and 2nd particles are sampled from a thermal distribution (left and right). However, to keep the sampling consistent with the sampling of correlated pairs, the 2nd particle is sampled from a similar restricted range (shown in green for the right plot).

4. Lastly, we calculate the correlation function $G^{(2)}(\Delta z)$ for both the generated correlated and uncorrelated pairs by histogramming the pair separations along the vertical axis (details in the next section). The normalised correlation function $g^{(2)}(\Delta z)$ is obtained by dividing the correlation function for correlated pairs by the function for uncorrelated pairs.

We use the above mentioned procedure to generate the pair-correlated data-set. However, an alternate approach (as suggested in the penultimate paragraph of the section on possible approaches) would be to repeatedly sample new particles from modified distribution. Although, when we tried implementing this scheme, we noticed that as the second particle gets sampled close to where the first particle landed, it enhances the probability of having the third particle land in the same local neighbourhood of the previous two particles. Moving further down the algorithm, the particles just tend to cluster together in a narrow

region creating a highly peaked probability distribution in that region (for instance, a narrow peak similar to the one in Fig 3.2 gets taller). This causes the particles sampled next in the sequence to ignore the broad thermal background which is now much smaller than the large peaked distribution, thus leading to a breakdown of this scheme to generate proper 2^{nd} order correlated data.

3.3 Calculation of the 2^{nd} order correlation function

Having generated the 2^{nd} order correlated data-set following previous sections with the appropriate parameters like trap frequencies, temperature and time of flight, we are ready to measure the 2^{nd} order correlation function. Recalling the definition for 2^{nd} order correlation function, the unnormalised correlation function is given by,

$$G^{(2)}(\mathbf{r}_1, \mathbf{r}_2) = \langle n_{\mathbf{r}_1} n_{\mathbf{r}_2} \rangle, \quad (3.10)$$

where the averaging in the definition represents ensemble average over the pairs of all particles. It is related to the joint detection probability of finding a particle at \mathbf{r}_2 given a particle at \mathbf{r}_1 . The normalised 2^{nd} order correlation function is given by,

$$g^{(2)}(\mathbf{r}_1, \mathbf{r}_2) = \frac{G^{(2)}(\mathbf{r}_1, \mathbf{r}_2)}{G^{(1)}(\mathbf{r}_1, \mathbf{r}_1)G^{(1)}(\mathbf{r}_2, \mathbf{r}_2)} = \frac{\langle n_{\mathbf{r}_1} n_{\mathbf{r}_2} \rangle}{\langle n_{\mathbf{r}_1} \rangle \langle n_{\mathbf{r}_2} \rangle}, \quad (3.11)$$

where the denominator consists of product of individual single particle densities, which are difficult to evaluate in an experiment. This is because it requires the precise knowledge of the local density, $n(\mathbf{r})$ in order to compute $\langle n(\mathbf{r}) \rangle = \int n(\mathbf{r}) d\mathbf{r} / V$ (which may vary with different runs of the same experiment as the atomic cloud moves). Alternately, a more convenient way to normalise $G^{(2)}(\mathbf{r}_1, \mathbf{r}_2)$ is to take the ratio between the correlation function for correlated pairs, $G_c^{(2)}(\mathbf{r}_1, \mathbf{r}_2)$ with the correlation function for uncorrelated pairs which factorises as, $G_u^{(2)}(\mathbf{r}_1, \mathbf{r}_2) = \langle n_{\mathbf{r}_1} \rangle \langle n_{\mathbf{r}_2} \rangle$. It is easier to determine $G_u^{(2)}$ experimentally (or numerically) by evaluating the $G^{(2)}$ for uncorrelated data. Hence, we work with the following form of definition for $g^{(2)}$,

$$g^{(2)}(\mathbf{r}_1, \mathbf{r}_2) = \frac{G_c^{(2)}(\mathbf{r}_1, \mathbf{r}_2)}{G_u^{(2)}(\mathbf{r}_1, \mathbf{r}_2)}. \quad (3.12)$$

In order to compute the correlation function $G^{(2)}$ one needs to histogram the pair separations between all possible pairs of particles in the ensembles, this would yield $G^{(2)}(\Delta r) \equiv G^{(2)}(0, \Delta r) = \langle n_{\mathbf{0}} n_{\Delta r} \rangle$ for a given pair separation Δr . However, this method of histogramming pairs in 3D presents some problems such as unequal sizes of histogram bins (the volume of a spherical shell bin of radius Δr scales as Δr^2).

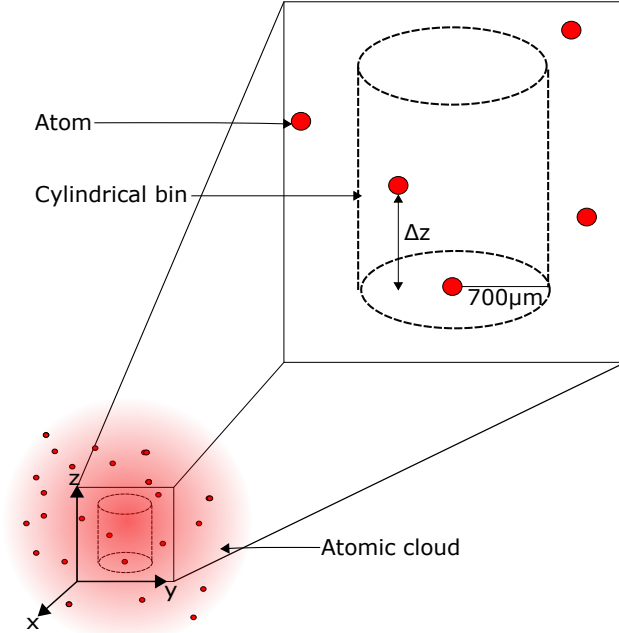


Figure 3.4: Binning the pair separations Δz for atoms lying within $700\mu m$ distance of the selected atom in the xy plane.

Hence to overcome the difficulty presented above, we histogram the pair separations in 1D along the vertical z-axis, as it has a better resolution ($\sim 10nm$) compared to x and y axes ($\sim 150\mu m$). To compute $G^{(2)}(\Delta z)$ we use the following binning scheme (Fig 3.4). For each atom in the generated correlated pairs, we check whether its partner lies within a $700\mu m$ radius bin in the xy plane, if so, we append its vertical separation Δz to a list. If the partner in the atom pair does not lie within the bin radius, the pair is discarded and we move to the next pair. The list of pair separations thus obtained is histogrammed with a bin size of $0.2l_z$ to obtain correlated $G_c^{(2)}(\Delta z)$. A similar histogram is made using the uncorrelated data-set to obtain the uncorrelated $G_u^{(2)}(\Delta z)$. Using the definition of $g^{(2)}$ as in Eq(3.12), we get the normalised second order correlation function $g^{(2)}(\Delta z)$.

3.4 Effect of finite detector resolution

In the computation of 2^{nd} order correlation function in the previous section, a perfect detector was assumed with arbitrarily low detector resolution. However, in practice the detector only has a finite resolution which need to be taken into account while estimating the reduction in the observed bunching amplitude in $g^{(2)}$ function. The effect of resolution can be modelled by a Gaussian smearing (of width d) of the particle position[13] (Fig 3.5). Numerically the resolution is incorporated by adding a Gaussian smear of width equal to the resolution of $\mathbf{d} = (0.01, 150, 150)\mu m$ to the particle positions of both correlated and uncorrelated data-sets.

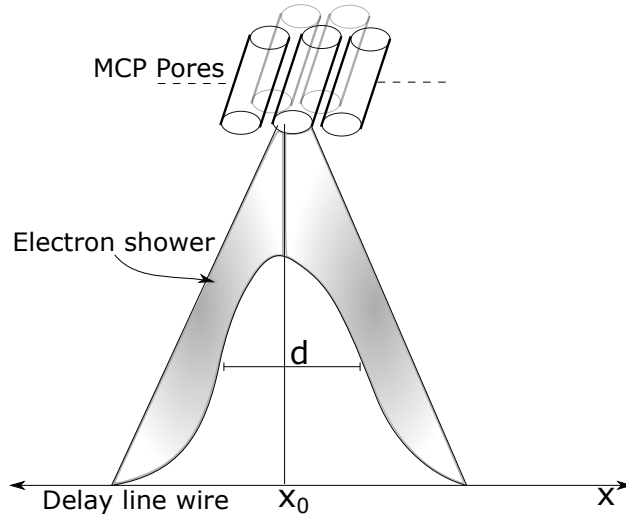


Figure 3.5: An oversimplified cartoon of how the Gaussian smearing of particle position due to electron shower between MCP and DLD detector (section 4.3) may affect the resolution.

According to this model[13], the effect of resolution is captured by convolving with the Gaussian resolution smear, $D(x, x_0) = \exp(-(x - x_0)^2/2d^2)/\sqrt{2\pi d^2}$. In a direction $\alpha = x$ with source size ‘ s ’ and correlation length ‘ l ’ at the detector, the in-trap density $\rho(x) = \rho_0 \cdot \exp(-x^2/2s^2)$ upon the Gaussian convolution becomes,

$$\rho_{obs}(x) = \int \rho(x_0)D(x, x_0)dx_0 = \frac{\rho_0}{\sqrt{1 + d^2/s^2}} \cdot e^{-x^2/2(s^2+d^2)}. \quad (3.13)$$

Similarly, the 1st order correlation, $G^{(1)}(x, x') = \rho_0 \cdot e^{-\frac{1}{2}(\frac{x+x'}{2s})^2} e^{-\frac{1}{2}(\frac{x-x'}{l})^2}$ scales as,

$$\begin{aligned} |G_{obs}^{(1)}(x, x')|^2 &= \int |G^{(1)}(x_0, x'_0)|^2 D(x, x_0) D(x', x'_0) dx_0 dx'_0 \\ &= \frac{\rho_0^2 e^{-\frac{(x+x')^2}{4(s^2+d^2)}} e^{-\frac{(x-x')^2}{(l^2+4d^2)}}}{\sqrt{1+d^2/s^2} \sqrt{1+4d^2/l^2}}. \end{aligned} \quad (3.14)$$

Thus the observed normalised second order correlation function is given by,

$$g_{obs}^{(2)}(0, 0) = 1 + \left| \frac{G_{obs}^{(1)}(0, 0)}{\rho_{obs}(0)} \right|^2 = 1 + \prod_{\alpha=x,y,z} \sqrt{\frac{1+d_\alpha^2/s_\alpha^2}{1+4d_\alpha^2/l_\alpha^2}}. \quad (3.15)$$

Hence, the observed width of the cloud in the direction α scales as $s_\alpha \rightarrow \sqrt{s_\alpha^2 + d_\alpha^2}$ and the correlation length increases as $l_\alpha \rightarrow \sqrt{l_\alpha^2 + 4d_\alpha^2}$, hence reducing the bunching amplitude (maximum value of HBT bunching) below $g^{(2)}(0, 0) = 2$. However, note that this model does not account for reduction in bunching amplitude due to binning.

As discussed in section 3.2 on the method for sampling particles, we fixed the cut-off length for sampling the second particle in step 2 to be bin width+ $3d$, where d is the resolution. This length is chosen such that the bin width roughly covers the distribution upto the correlation length, with the additional three standard deviations $3d$ covering about 99% of the distribution under the resolution smearing Gaussian.

3.5 Benchmarking the simulation

We benchmark our code for generating a correlated data-set (as discussed in the previous sections) by attempting to reproduce the experimentally observed bunching excess and correlation lengths for the experimental parameters as in [16]. We generate data for a thermal cloud of 10^7 correlated pairs of atoms at various temperatures (including $T=1.3\mu K$ as in [16]), magnetic trap frequencies $(\omega_x, \omega_y, \omega_z) = (51Hz, 565Hz, 565Hz)$, time of flight $t_{TOF}=0.416$ s and a detector resolution of RMS width $d = 150\mu m$ in the XY-plane. This is followed by the generation of 10^7 uncorrelated pairs for normalisation.

The second order correlation functions $G^{(2)}(\Delta z)$ and $g^{(2)}(\Delta z)$ are then calculated by histogramming the pair separations using the procedure described in section 3.3. The ex-

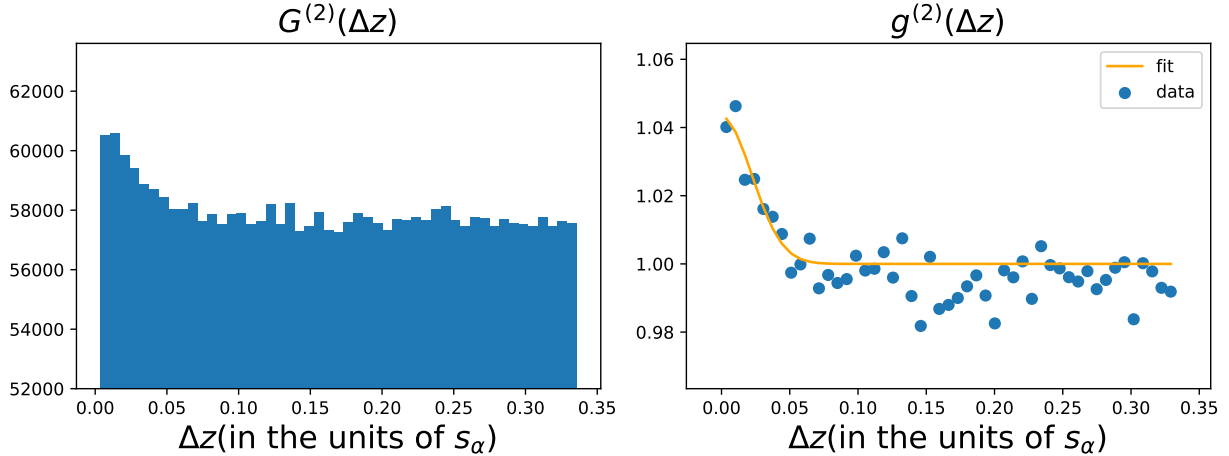


Figure 3.6: Unnormalised (left) and normalised (right) 2^{nd} order correlation functions for a thermal cloud at $T=800$ nK. We have shown the plot for $T=800$ nK (as a representative) instead of $T=1.3\mu K$ (which we intend to reproduce) as the bunching peak is much bigger and clearer to see at $T = 800nK$.

pression for the second order correlation function (Eq 2.18, or Eq2.25 for the atomic variant) is given by $g^{(2)}(\Delta x, \Delta y, \Delta z) = 1 + \exp\left(-\frac{\Delta x^2}{l_x^2} - \frac{\Delta y^2}{l_y^2} - \frac{\Delta z^2}{l_z^2}\right)$. Hence we fit $g^{(2)}(\Delta z)$ to the following form

$$g^{(2)}(\Delta z) = 1 + \eta \cdot \exp\left(-\frac{\Delta z^2}{l_z^2}\right), \quad (3.16)$$

With the free parameter η quantifying the bunching excess and l_z being the correlation length along the z-axis (vertical direction). Fig 3.6 shows a plot for simulation of unnormalised and normalised 2^{nd} order correlation functions for an atomic cloud at $T = 800nK$. Observe that the bunching amplitude expected from theory (Hanbury Brown and Twiss effect for thermal bosons, that is $g^{(2)}(0) = 2$) is clearly reduced in the plot to $g^{(2)}(0) = 1.04(2)$ instead. The reduction in bunching excess for thermal bosons can be attributed to the following physical or experimental factors:

1. **Binning of data:** While histogramming the pair separations along the z axis, we only considered correlations among particles which lie “close by” in the xy plane by using a cylindrical bin (Fig 3.4). The particles that lie in the xy plane contribute to the bunching excess η by the factor $\exp(-\Delta x^2/l_x^2 - \Delta y^2/l_y^2)$ (Eq 3.16). Choosing a small enough bin (equivalently $\Delta x \ll l_x$ and $\Delta y \ll l_y$) would prevent the suppression in bunching excess at the cost of less pairs per bin, hence increasing the time required

to run the simulation. On the other hand, if the bin size is large, it would have an averaging effect that would reduce the bunching excess; however, we gain signal-to-noise by having more pairs per bin. Hence, an optimal bin size should be comparable to the correlation lengths, which in this case are $l_x \sim 40\mu m$ and $l_y \sim 450\mu m$ at $1.3\mu K$. The experiment[16] we are trying to reproduce chooses a bin size of $700\mu m$ (and so do we) although their detector resolution ($150\mu m$) is much smaller than this.

2. **Detector resolution:** As discussed in section 3.4, the effect of detector resolution can be modelled by adding a Gaussian smear to the particle positions. Thus this smearing of data due to resolution can reduce the bunching excess. Upon assuming ideal binning (one which doesn't affect the bunching), the bunching excess η due to finite detector resolution is given by (cf Eq 3.15)

$$\eta = \prod_{\alpha} \sqrt{\frac{1 + d_{\alpha}^2/s_{\alpha}^2}{1 + 4d_{\alpha}^2/(l_{\alpha}^{(d)})^2}}. \quad (3.17)$$

Setting the RMS width of the detector resolution for experiment[16], $d = 150\mu m$ in the above formula gives a bunching excess $\eta = 0.11$ which overestimates the value $\eta = 0.022(2)$ as observed in the experiment by a factor of 5. This is because the reduction in bunching due to binning (as discussed in point 1 above) is not accounted for while calculating η in Eq 3.17.

3. **Formation of condensate:** After crossing the critical temperature for Bose-Einstein condensation, the condensate density $\rho_0(\mathbf{r})$ cannot be ignored (cf Eq 2.26) in the expression for $G^{(2)}$ function. This results in the $g^{(2)}(0, 0)$ given by

$$g^{(2)}(0, 0) = \frac{G^{(2)}(0, 0)}{\rho(0)\rho(0)} = 1 - \frac{\rho_0(0)\rho_0(0)}{\rho(0)\rho(0)} + \cancel{|g^{(1)}(0, 0)|^2} \rightarrow 1 \quad (3.18)$$

Thus the condensate density term (with $\rho_0(0)$) is capable of pulling down the value of $g^{(2)}(0, 0)$ below 2. However, In our case, this factor is not applicable as we are simulating a thermal cloud of atoms above the critical temperature.

We simulate the correlation functions for a couple of temperatures including $T = 1.3\mu K$ in order to observe the scaling of correlation function with temperature (and to compare it with theoretical scaling). The simulation results for scaling of correlation length and bunching excess with temperatures ranging from $0.1\mu K$ - $10\mu K$ are summarized in Fig 3.7.

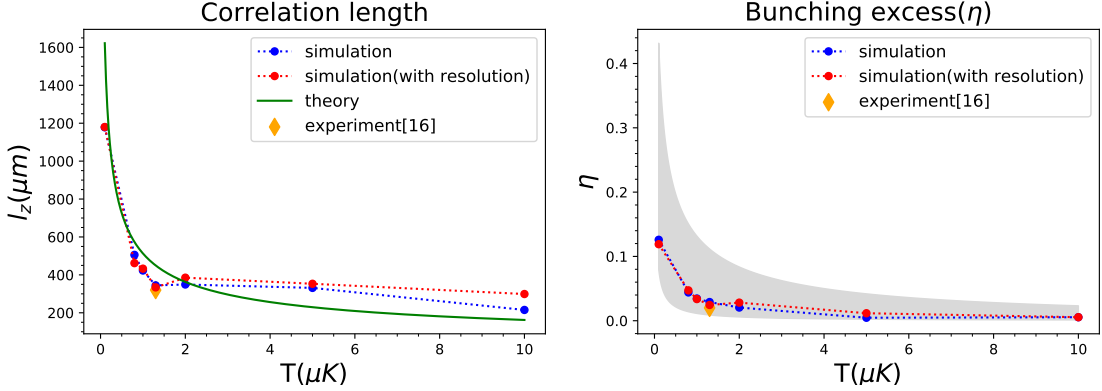


Figure 3.7: Scaling of correlation length and bunching excess with temperature obtained from simulation. The orange diamond shows the experimental values[16] for the respective plots. The grey shaded region represents the theoretical bounds on bunching excess due to resolution as discussed in the last paragraph.

These plots are obtained by generating a 2^{nd} order correlated data-set with fixed system parameters as used in experiment[16] at different temperatures (Fig 3.6 shows a plot for $T = 800nK$ for instance) and fitting it to Eq 3.16. The fitting gives us the correlation length l_z and the bunching excess η . For each temperature, we average over 4 data-sets. In Fig 3.7, the left plot represents the correlation length of l_z obtained from simulation with the incorporation of resolution (Red line) compared to one without accounting for the resolution (Blue line). Recall that the correlation length at a given temperature T (Eq 3.3) scales as $1/\sqrt{T}$ which is plotted as the green line.

For $T = 1.3\mu K$ the experiment[16] obtains a value of correlation time of $t = 90(10)\mu s$ which can be converted to correlation length by multiplying with the velocity of the centre of mass of the atomic cloud as it hits the detector, $v = gt_{TOF} \approx 4m/s$, giving a correlation length of $l_z = vt = 360(40)\mu m$. From our simulation, we obtain $l_z = 370(60)\mu m$. Similarly, the right plot in Fig 3.7 represents the fit values for bunching excess η obtained from simulation with and without resolution, respectively. The experiment[16] measures a bunching excess of $\eta = 0.022(2)$ and the simulation gives a bunching excess of $\eta = 0.029(5)$. The uncertainties in the simulation values for η and l_z represent the standard deviation of the 4 data sets obtained from the simulation. The results are summarised in table 3.1.

From the plots in Fig 3.7, it seems that incorporating detector resolution into the simulation has little effect on both correlation length and bunching excess. This could be because the reduction in bunching caused by binning the data in $700\mu m$ bins may dominate the

	Bunching Excess(η)	Correlation length(l_z in μm)
Simulation	0.029(5)	370(60)
Theory[16]	0.025(5)	320(80)
Experiment[16]	0.022(2)	360(40)

Table 3.1: Simulation and experimental values[16] (with theoretical estimates) for bunching excess and correlation length at $1.3\mu K$.

reduction in bunching due to the detector resolution of $150\mu m$. However, we can still use the resolution of $d = 150\mu m$ in Eq 3.15 to obtain a rough theoretical upper bound for the expected bunching due to the finite resolution of the detector. Similarly, we can obtain a lower bound for bunching by considering the extreme case with a detector resolution comparable to the bin size, that is $d = 700\mu m$. In Fig 3.7, the grey shaded region in the plot for bunching excess represents the range of possible values of bunching excess calculated using Eq 3.17 with $150\mu m < d < 700\mu m$ as discussed above.

3.6 Results: Expected bunching in our setup

Having benchmarked the simulation in the previous section, we repeat the simulation with the trap parameters of our crossed optical dipole trap. We use the simulation to estimate the 2^{nd} order correlation expected from our system of He* atoms with temperature $T = 13\mu K$ trapped in a crossed optical dipole trap with trap frequencies $(\omega_x, \omega_y, \omega_z) = (1190Hz, 600Hz, 1340Hz)$, time of flight $t_{TOF}=0.298$ s and a detector resolution of RMS width $d = 150\mu m$ in the XY-plane. For the purpose of the simulation, 10^7 correlated and uncorrelated pairs are generated. Note that the above-mentioned trap frequencies are calculated by using the powers in the beams of the dipole trap (by fitting a parabola to the potential U obtained from Eq 1.19) and are yet to be experimentally measured. The following plots in Fig 3.8 shows the simulation result for 2^{nd} order correlation function with our system parameters as mentioned above.

We obtain the following values (Table 3.2) for the expected bunching excess and correlation length after averaging over 5 runs of simulations. Where the theoretical upper and lower bounds for η are found using Eq 3.17 with the resolutions $d = 150\mu m$ and $d = 700\mu m$ respectively following similar considerations as in section 3.5. Hence it is reasonable to as-

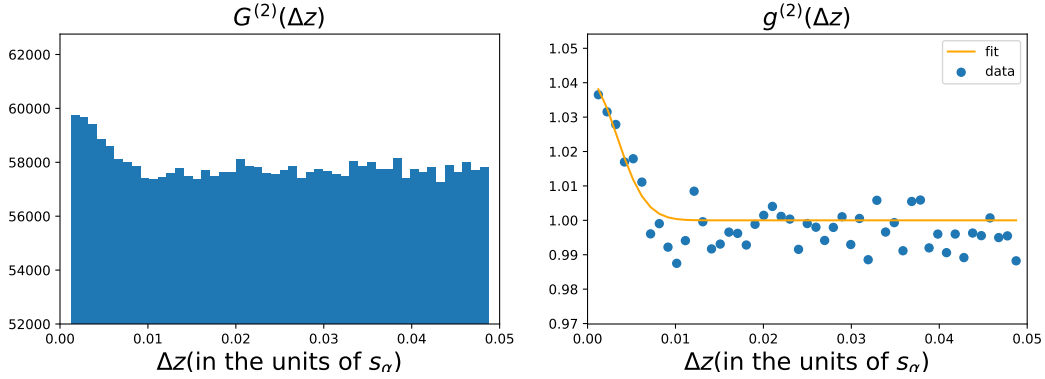


Figure 3.8: Unnormalised (left) and normalised (right) 2^{nd} order correlation functions for thermal atoms in optical dipole trap.

	Bunching Excess(η)	Correlation length(l_z in μm)
Simulation	0.040(4)	220(20)
Theory [Eq 3.17,3.3]	0.011-0.196	240

Table 3.2: Simulation and theory values for expected bunching excess and correlation length for our system of thermal atoms in optical dipole trap.

sume that we can observe the bunching effect from the thermal cloud in our optical dipole trap frequencies with the given detector resolution. Furthermore, we could optimise the experimental sequence to compress the optical dipole trap after evaporation, which would increase the trap frequencies and hence the correlation length, make the bunching even more apparent. Additionally, the observed bunching could also be increased by using a smaller bin size (compared to the currently used $700\mu m$ bin-size).

Chapter 4

Experimental Methods and Results

4.1 The He* BEC Apparatus

In section 1.2, we discussed the physical principles involved in cooling and trapping atoms, we now use these to describe the process involved in cooling and trapping He* atoms followed by the formation of BEC of He* atoms[8].

The procedure for cooling He* atoms to achieve a Bose-Einstein condensate begins with a discharge source which produces He* atoms moving at high velocities of the order 1000m/s. These atoms are slowed down to velocities of the order 10cm/s by passing through various cooling and trapping stages as a part of the He* BEC apparatus (Fig 4.1) to reach the condensate phase.

The first stage of the apparatus consists of a high voltage cryogenically cooled DC discharge source which excites the gas of He atoms to various excited states due to bombardment with high energy electrons. The source is cooled by liquid nitrogen for the removal of excess heat generated by the discharge and collision process, and it cools the atoms down to liquid nitrogen temperatures ($\sim 77K$). From this soup of He excited states, electrons and ions present in the source chamber, we are only interested in trapping atoms in the 1st excited (metastable) state which constitutes only a tiny fraction($\sim 10^{-4}$ to 10^{-5})[8] of the total number of particles. As only the He* atoms interact with 1083nm laser light resonant with the laser cooling transition for He* atoms, these atoms can be selectively targeted and separated

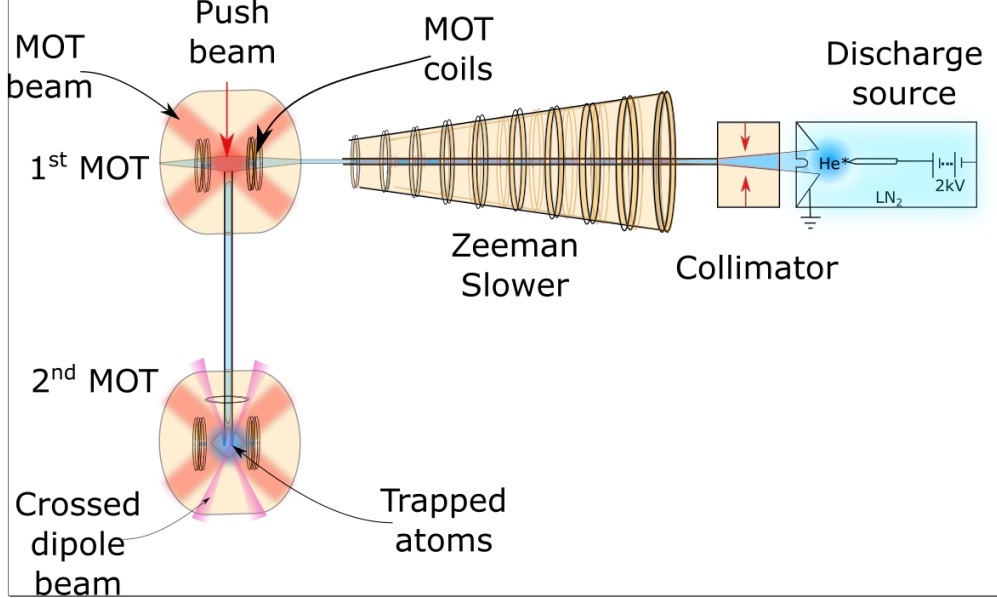


Figure 4.1: A schematic diagram of the He* BEC apparatus

from the rest of the excited states by using this laser.

The atomic flux is then passed through a collimator which consists of two pairs of counter-propagating red-detuned laser beams in the directions orthogonal to the axis of the He* flux. It helps in reducing the velocities in the directions transverse to the desired direction of propagation. The collimated flux is then fed into a Zeeman slower which slows down the atoms from about 1000m/s to about 100m/s. As the atoms slow down, the Doppler shift needs to be readjusted to match the resonance condition, which is achieved by a variable magnetic field produced by the Zeeman slowing coils (as discussed in section 1.2.1).

After slowing down an order of magnitude in velocities from the source to Zeeman slower, the atomic flux then enters the magneto-optical trap (MOT) which plays a crucial role in the production of BEC by simultaneously cooling and trapping the atoms (section 1.2.2). In our case we have two MOTs instead of one as the velocities of atoms in the 1st MOT are still high enough ($\sim 100 - 10m/s$) for effectively capturing the atoms. To achieve high loading rate and low two-body losses due to Penning ionisation, the MOT consists of laser beams with large waists to have a large capture fraction, and it operates at low-density conditions to prevent the losses. The density is increased after cooling by compressing the MOT.

The cooling in the MOT is insufficient to increase phase space density ($\sim NT^{-3/2}$)

beyond its critical value for Bose-Einstein condensation. Hence, the cold atoms ($\sim 1mK$ temperature) from the MOT are transferred to a conservative trapping potential such as a magnetic trap for in-trap cooling, followed by an optical dipole trap for evaporative cooling. In the case of an optical dipole trap, the height of the trap is lowered to allow the high energy atoms to escape the trap, leaving behind atoms with a lower temperature. This gives a high enough phase space density to achieve a quantum phase transition to a BEC.

4.2 Temperature estimation

We can estimate the temperature of a trapped atomic cloud by using a technique known as *absorption imaging*. In this technique, a low-intensity near-resonant beam ($\lambda = 1083nm$) is shone on an atomic cloud and an image of the shadow cast by the cloud after absorbing the light is captured by a CCD camera (Fig 4.2 (a)). A similar image without the atomic cloud is taken a few milliseconds after the first image (Fig 4.2 (b)). These images are filtered by subtracting a reference image taken by blocking the Zeeman slower (i.e. with no atoms trapped), this subtracts off the noise due to factors like scattered light, beam movement, etc and we obtain a clearer image (Fig 4.2 (c) and (d)).

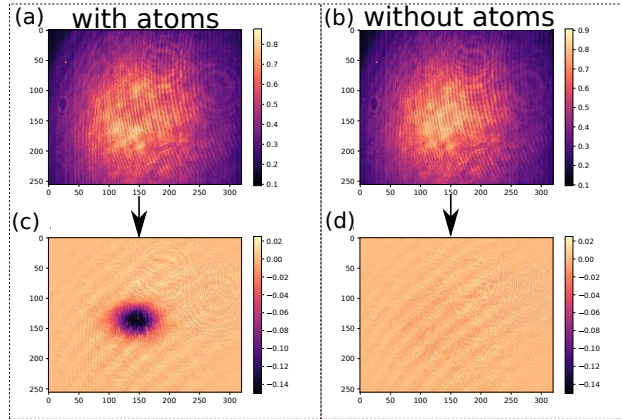


Figure 4.2: (a) image with cloud (b) image without cloud. (c) and (d) represent background subtracted images for (a) and (b) respectively. The xy axis represents camera pixels.

Beer's law states that light intensity decreases exponentially from I_0 to I after travelling through a medium of optical density OD , that is, $I = I_0 \exp(-OD)$. Thus the optical density of the medium is given by

$$OD = \log\left(\frac{I_0}{I}\right). \quad (4.1)$$

We use the 2D intensity profile for the absorption images with the cloud, I and without the cloud, I_0 to compute the optical density profile. This profile is then used to fit a 2D-Gaussian along the r and z axes as shown in Fig 4.3 which contains the OD profile for an atomic cloud trapped in a magnetic trap. The Gaussian widths of the cloud can be used to determine the temperature after a time of flight measurement. For the time of flight measurement, we release the atoms from the trap to free fall under gravity for a fixed interval of time, during which the cloud expands with an RMS velocity $v = \sqrt{k_B T/m}$ in each direction. This expansion of the cloud in a given direction with an initial width of σ_0 for a time of flight (TOF) t is given by

$$\sigma = \sqrt{\sigma_0^2 + v^2 \cdot t^2}. \quad (4.2)$$

Thus by measuring the width of the cloud after several time of flight measurements, one can obtain the temperature by fitting σ vs t .

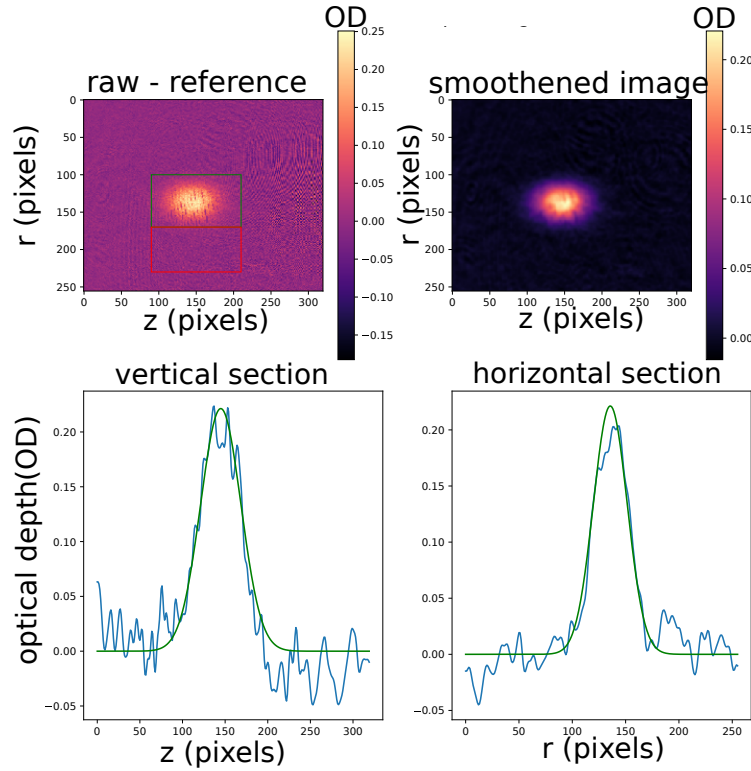


Figure 4.3: Typical optical density profile for atoms trapped in a magnetic trap. The two plots on the top show the optical density profile (with raw image on the left and smoothered image on the right), the bottom panel shows the Gaussian fit along z and r axes (1 pixel= $20\mu m$).

4.2.1 Results: Absorption imaging

Using absorption imaging as discussed in section 4.2, we estimate the temperature of the cloud in the magnetic trap (with and without in-trap cooling) by using the technique of absorption imaging.

We take the absorption images for the atomic cloud in the magnetic trap (in situ) and after dropping the cloud from the magnetic trap for various time of flights ranging from 0 to 2ms. This is done for two different cases, namely, with 400ms of in-trap cooling present and with in-trap cooling switched off respectively. We then obtain the widths of the expanded clouds at a different time of flights by fitting the Gaussian optical density profile (see Fig 4.3 for example). The two Gaussian widths σ_z and σ_r along the vertical (z) and horizontal (r) direction respectively are plotted with respect to time of flight to obtain the temperature using Eq 4.2 for $\sigma = \sigma_z$ and $\sigma = \sigma_r$. Fig 4.5 shows the results for σ_z and σ_r vs time of flight t for the atomic cloud in magnetic trap without in-trap cooling, with Fig 4.4 showing a few representative atomic cloud images (optical densities) for different time of flights.

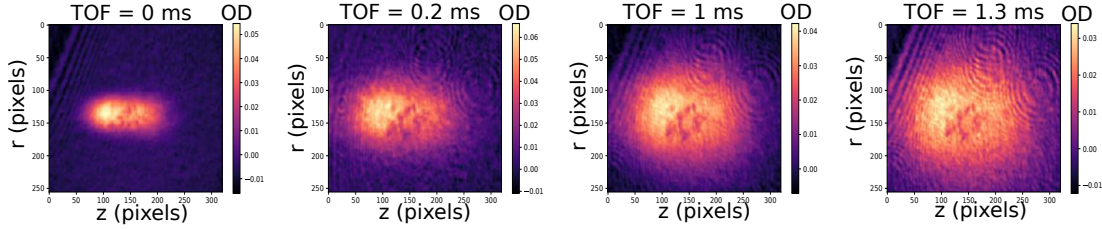
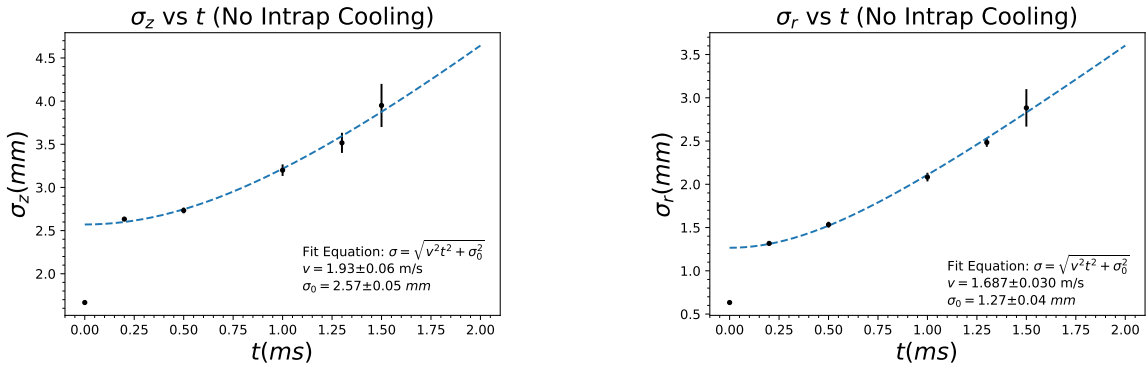


Figure 4.4: Time of flight profile without in-trap cooling (1 pixel = $20\mu\text{m}$).



(a) cloud widths in vertical direction.

(b) cloud widths in horizontal direction.

Figure 4.5: Cloud widths vs time of flight with no in-trap cooling.

The error bars on the plots (4.5) represent the data points for 2 sets of measurements at a given time of flight. The first point with zero time of flight (in situ) is not used for a fitting because it is imaged in the presence of a magnetic field in the magnetic trap and all the others are time of flight measurements after magnetic trap switch off. Furthermore, the widths of the in situ cloud seem to lie below the fit intercept σ_0 , a reason for this can be that the laser beam in the magnetic trap is resonant only with some fraction of the cloud; hence we can image only that fraction. Similarly, we plot the data for the atomic cloud with 400ms of the in-trap cooling stage (that is by shining a red-detuned vertical laser beam for 400ms before switching off the magnetic trap) as shown in Fig 4.6 and Fig 4.7. A possible reason for the asymmetric expansion along the z and r axes of the cloud as seen in the Fig 4.6 could be because the in-trap cooling beam may be compressing the cloud along the z axis (in the image). This may also suggest that the cloud didn't have sufficient time to re-thermalise, leading to different temperature measurements along different directions (table 4.1).

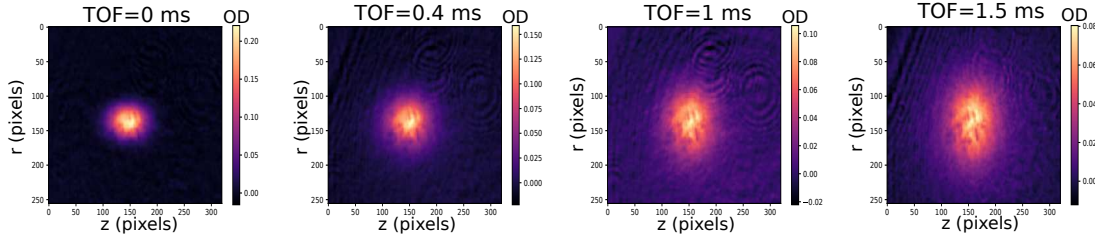
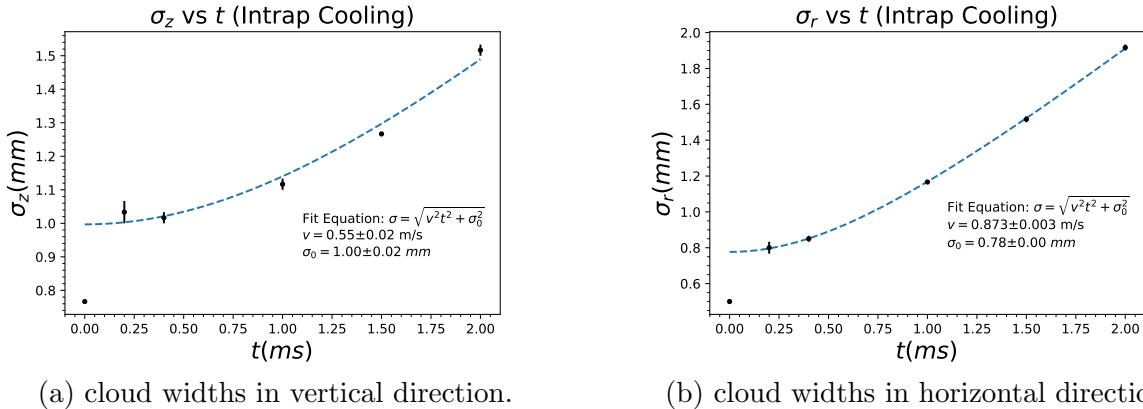


Figure 4.6: Time of flight profile with in-trap cooling (1 pixel = $20\mu m$).



(a) cloud widths in vertical direction.

(b) cloud widths in horizontal direction.

Figure 4.7: Cloud widths vs time of flight with in-trap cooling.

Using the RMS velocities (obtained from fitting) we obtain the following temperature of the atomic clouds with and without in-trap cooling as presented in Table 4.1. Thus we see that the in-trap cooling stage cools the atoms by about a factor of 8 from $T \sim 1.6mK$

without in-trap cooling to $T \sim 260\mu K$ with in-trap cooling.

axis	No in-trap cooling		in-trap cooling	
	z	r	z	r
v (in m/s)	1.93(6)	1.69(3)	0.55(2)	0.873(3)
T (in μK)	1800(60)	1380(25)	150(5)	370(1)
mean T (in μK)	1600(60)		260(5)	

Table 4.1: Temperatures with and without in-trap cooling.

4.3 Far-field single atom detection

The single-atom detection capability offered by meta-stable helium enables us to reconstruct the 3D profile of the cold atomic cloud. Using this profile, one can easily calculate the second-order correlation function (or any order in general) by histogramming the particle pair separations along the z -axis as discussed in section 3.3. Throughout the rest of this thesis, we refer to the process of a particle hitting the detector as an *event*.

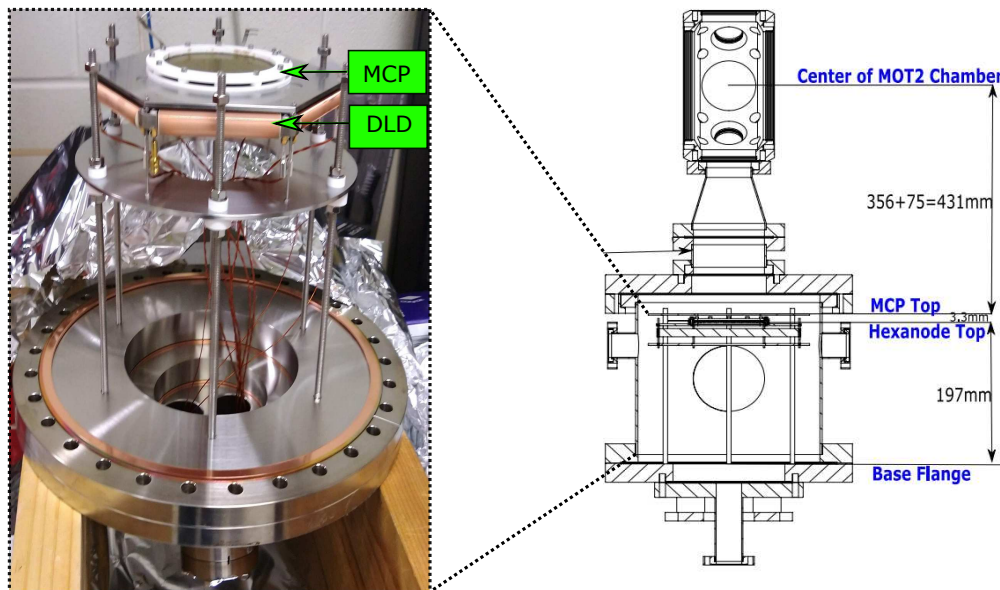


Figure 4.8: The microchannel plate and delay-line detector (left) with cross section of vacuum chamber hosting the detector (right), with the detector sitting below the 2nd MOT chamber (Fig 4.1).

The detector apparatus for performing the far-field single-atom detection (and hence the correlation function measurement) consists of a microchannel plate (MCP) and a delay line detector (DLD) along with other auxiliary electronics (Fig 4.8). The raw data in the form of pulse arrival times being output from the apparatus is reconstructed into meaningful events of the location of atoms hitting the delay line detector using a script on the computer. Once the events are reconstructed, another script can be used to calculate the second-order correlation function (we have written the script but haven't computed the correlation function due to some technical issue as discussed in section 4.3.5). In this section, we will briefly discuss about each of the above components involved in the far-field single atom detection (and hence the correlation function measurement).

4.3.1 Microchannel plates (MCP)

The microchannel plates are a pair of 80mm wide stacked discs with an array of $12\mu\text{m}$ diameter pores with each pore acting as an electron multiplier (Fig 4.9). In an event of a He^* atom hitting the MCP surface, one or more electrons are ejected from the surface by releasing the high internal energy of the He^* atom ($\sim 20\text{eV}$) which is greater than the work function for typical metals ($\sim 5\text{eV}$). The 'primary' electron(s) triggers a shower of other secondary electrons to be ejected down the MCP pore, thus amplifying the electron(s) to a obtain a measurable current. The potential difference of 2.05kV between the front and back faces of the MCP sets the amplification factor ($\sim 10^7$ [28]).

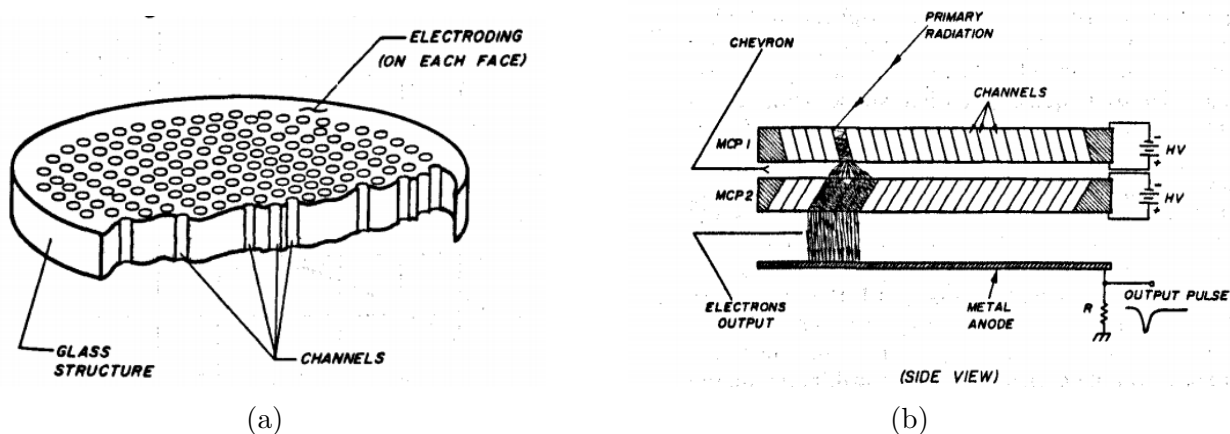


Figure 4.9: (a) Cross section of a microchannel plate (MCP). (b) Two MCPs stacked in chevron (or V-shape) configuration (image source: [27]).

In order to extract the spatial location and timing of the event, the current from the MCP is directed towards the DLD. However, even by itself, the MCP is a useful tool to electronically detect the count rate of He^* atoms and ions falling onto its surface. One can measure the time of flight profile even for a very small number of atoms (say released from the optical dipole trap) due to the single-atom detection capabilities, which is not usually measurable by saturated absorption imaging (section 4.2), as that requires a larger number of atoms for absorbing sufficient amount of light. On dropping a cold gas of atoms (below its critical temperature for condensation) on the MCPs, the time of flight (TOF) obtained provides a useful method to find the condensate fraction of the cloud by fitting the TOF peak to a Thomas-Fermi profile with a thermal tail (as discussed in the following section 4.3.2).

Estimating the quantum efficiency of the MCPs

When the particles hit the MCPs, only a fraction of them get converted to counts on the MCP. This fraction is known as the quantum efficiency (QE) of the detector. The QE is an important parameter for the MCP which helps one convert the counts obtained on the MCP to the number of atoms falling on the MCP. To determine the number of atoms falling on the MCPs, we need to take into account the geometry of the MCPs and the spatial extent of the atomic gas (Fig 4.10). We calibrate the total number of atoms falling on the MCP from the MOT by measuring MOT fluorescence, which yields $\sim 1.2 \times 10^8$ atoms at $\sim 1\text{mK}$ (obtained from absorption imaging).

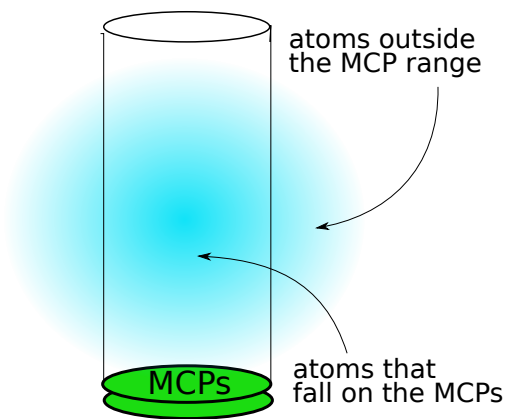


Figure 4.10: Out of the total atoms (blue) released from the MOT, only a fraction of atoms in the cylindrical region above the 80mm diameter MCPs are incident on the MCP surface.

The fraction of atoms, f , of the total number of atoms from the MOT that actually hit the MCPs is given by

$$f = \frac{\int_{MCP} dx \cdot dy \cdot dz \cdot \exp\left(-\frac{x^2+y^2+z^2}{2\sigma^2}\right)}{\int_{Total} dx \cdot dy \cdot dz \cdot \exp\left(-\frac{x^2+y^2+z^2}{2\sigma^2}\right)} = \frac{\int_0^{4cm} r dr \cdot \exp\left(-\frac{r^2}{2\sigma^2}\right)}{\int_0^\infty r dr \cdot \exp\left(-\frac{r^2}{2\sigma^2}\right)} = 1 - e^{-8cm^2/\sigma^2}, \quad (4.3)$$

where, atoms are assumed to occupy Boltzmann distribution at a temperature T with the width, $\sigma = \sqrt{k_B T / m t_{TOF}}$ and the time of flight $t_{TOF} = 0.29s$. At $1mK$, the width of the atomic cloud, $\sigma = 43cm$ is larger than the MCP diameter of $8cm$, with $f = 0.034$. Thus the fraction of atoms falling on the MCPs = $f \times 1.2 \times 10^8 = 4.08 \times 10^6$ atoms. However the MCP registers $\sim 2.3 \times 10^5$ counts. Thus quantum efficiency is estimated to be

$$QE = \frac{MCP \text{ counts}}{No. of atoms falling on MCP} = \frac{2.3 \times 10^5}{4.08 \times 10^6} = 5.6\% \quad (4.4)$$

4.3.2 Results: Time of flight signal from MCP

In this section, we present a typical time of flight trace obtained from the MCP, followed by a discussion of the bi-modal distribution (of BEC and thermal atoms) that indicates the onset of BEC. The following plot, Fig 4.11, represents a trace of spatially integrated (over x-y plane) count rate of our experimental sequence for loading the optical dipole trap and producing a BEC of He*.

The plot can be divided into 4 sections of interest,

1. **MOT loading:** The first broad signal occurring between $t=0$ to $1s$ represent MOT loading. As the He* atoms enter the MOT, they undergo collisions among themselves (Penning ionisation) as well as the walls of the vacuum chamber. This leads to ionisation of He* atoms which is registered as the broad ion signal on the MCP.
2. **Untrapped atoms from the magnetic trap:** The first big peak occurring close to $1.5s$ in the sequence occurs because during this time we are in the process of transferring atoms from the MOT to a magnetic trap. The magnetic trap can only confine the low field seekers, $m_J = 1$ sublevel and the remaining atoms in the $m_J = 0, -1$ sublevels fall out of the trap and register a peak close to $t=1.5s$.

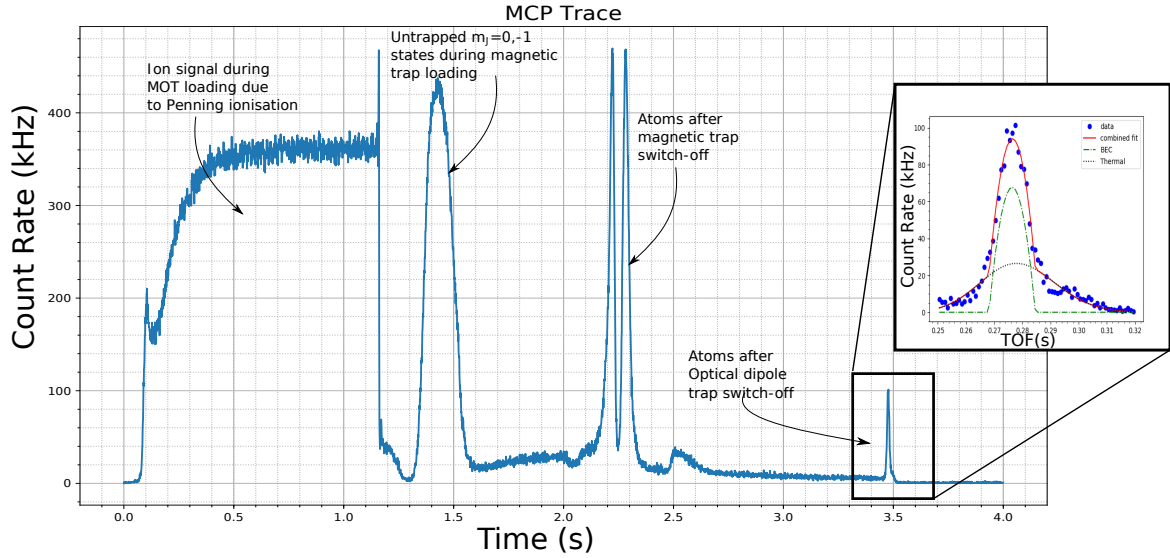


Figure 4.11: MCP Trace for optical dipole trap loading to from condensate followed by a time of flight measurement.

3. **Magnetic trap ramp down:** The second big peak occurs close to $t=2.2-2.3$ s. Although this ‘M’ shaped feature looks like twin peaks, however, it is just a single peak that has saturated the MCPs, burning a hole at the centre of the peak. The hole is filled after the MCPs regain their charge, which is seen as the 2nd peak of the ‘M’ shape. The peak occurs after we ramp down and switch off the magnetic trap, which releases the He* atoms that are not captured by the dipole trap and fall onto the MCP giving this peak.
4. **Optical dipole trap switch off:** From the magnetic trap, the atoms are transferred to a tighter optical dipole potential (with larger trap frequencies) in order to evaporatively cool the atoms to degeneracy and obtain a Bose-Einstein condensate. After evaporative cooling, achieved by lowering the optical potential, we are left with a finite fraction of atoms in the condensate phase, which are detected on the MCP by switching off the optical dipole trap. We then fit this time of flight profile to a bi-modal distribution (details in the following section) consisting of a Thomas-Fermi distribution for the BEC fraction and a Boltzmann distribution for the thermal fraction as shown in the inset (zoomed in on the peak).

Fitting the bi-modal distribution

We fit the peak from the optical dipole trap switch off, Fig 4.11, as is shown in the following Fig 4.12 with a bi-modal distribution. The bi-modal distribution represents a Thomas-Fermi fit (section 1.1.2) for the BEC fraction and a Maxwell-Boltzmann fit to the thermal fraction. This is an important plot which shows the onset of BEC. To obtain the temperature from the thermal part of the cloud, we fit it to a Maxwell-Boltzmann distribution spatially integrated in XY to give count rate of atoms as a function of time given by [23],

$$n(t) = \pi v_{mp}^2 \left(\frac{m}{2\pi k_B T} \right)^{3/2} \left(\frac{l_0 + gt^2/2}{t^2} \right) \exp\left(- \frac{(l_0 - gt^2/2)^2}{v_{mp}^2 t^2} \right), \quad (4.5)$$

where, m is the mass of He, T is the temperature, l_0 is the falling distance, $v_{mp} = \sqrt{2k_B T/m}$ is the most probable thermal velocity and t is the time of flight. From this fitting we obtain a temperature of $8\mu K$ for the cloud. Given the trap frequencies used for the optical dipole trap of $(725, 370, 815)Hz$ and the total atom numbers $N = 1.6 \times 10^5$, we obtain a critical temperature[24] of $T_c = 0.94\hbar\tilde{\omega}N^{1/3}/k_B = 9.96\mu K$, where $\tilde{\omega}$ is the geometric mean of the trap frequencies. We obtain a condensate fraction of $N_0/N = 0.46$, where N_0 and N are the

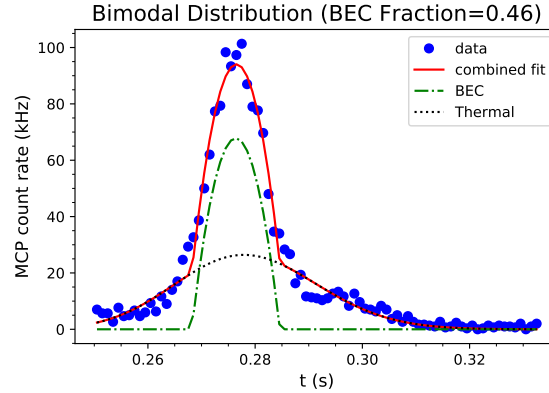


Figure 4.12: Bi-modal fit for the BEC fraction (Green) and the thermal fraction (Black).

number of atoms in the BEC and the total number of atoms respectively. The numbers, N_0 , N are proportional to the area under the curve for BEC fit and the combined fit respectively. Furthermore, as discussed in section 1.1.2, we fit the BEC fraction to a Thomas-Fermi distribution with Thomas-Fermi radius $\sim 2cm$ (which reflects the momentum width in far-field after trap switch-off).

4.3.3 Delay line detector(DLD)

The MCP is useful for getting a spatially integrated time of flight profile for particles falling on its surface. However, in order to compute correlation functions such as the 2^{nd} order correlation function, one also needs be able to spatially resolve the location of individual particles in the XY plane (as required by the binning scheme in Fig 3.4). This is where the delay line detector is useful to spatially resolve the particle positions in the XY plane, with the fall time on the detector giving location along the Z axis.

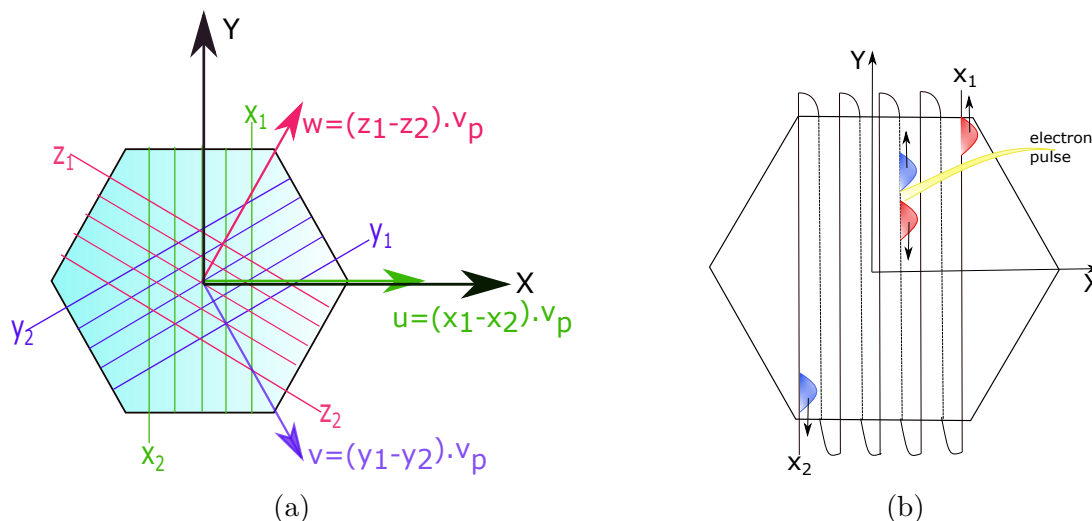


Figure 4.13: (a) Hexagonal (u,v,w) and Cartesian (X,Y) coordinates on the DLD. The 3 wires shown in pink, green and purple are wound at an angle of 60° with each other. (b) Pulse propagation on a single winding of DLD. Location of an event is inferred from the arrival time difference between x_1 and x_2 .

The Hexanode delay line detector consists of 3 wires wrapped along a hexagonal disc (only one of the 3 wires in Fig 4.13a is shown in Fig.4.13b), each wire has two ends (labelled x_1 and x_2 in this case). When the electron shower from the MCP strikes a wire, it causes two pulses to travel in either direction along the wire (blue and red pluses in Fig. 4.13b). Based on the difference in arrival times of the signals at both ends of the wire ($x_1 - x_2$), one can spatially pinpoint the location of the event of a He^* atom hitting the detector along the axis perpendicular to the direction of the wire winding. For instance, when the difference in arrival times is 0, we know that the event should have occurred at the mid-point of the wire and when the time difference takes its maximum possible value, the event can be located at the edge of the detector. Perpendicular to the wire windings as shown in Fig 4.13b, the event can be located at $(x_1 - x_2) \cdot v_{px}$, where v_{px} is the velocity of propagation of the pulse in the

direction perpendicular to the wire, which is typically of the order $\sim 1\text{mm/ns}$. Similarly, arrival times on the remaining two wires yields the following location (Fig 4.13a),

$$\begin{aligned} u &= (x_1 - x_2) \cdot v_{px} \\ v &= (y_1 - y_2) \cdot v_{py} \\ w &= (z_1 - z_2) \cdot v_{pz} + o, \end{aligned} \tag{4.6}$$

where $v_{pi}, i = x, y, z$ are the velocities of propagation for the corresponding wires, which in general may be different considering that the lengths of the wires are slightly different. o represents an offset which can be fixed by comparing u, v, w for the same event. Another important quantity to consider is the time taken for a pulse to traverse the entire length of the wire, known as the T_{sum} , which sets a time-scale for the reconstruction of the events.

To locate the event (atom hitting the detector) in the XY plane, we can use the location of the event on any two of the three wires of the DLD (which is nice because we have redundant information which can be used in case of missing pulse on up to 3 out of the 6 ends of the wires). The positions u, v, w are given in the hexagonal coordinates system which can be transformed back into the usual XY coordinates in three possible ways depending on the choice of two out of three hexagonal coordinates (u, v, w) . A simple coordinate transformation yields the following:

$$\begin{aligned} X_{uv} &= u, \\ Y_{uv} &= (u - 2v)/\sqrt{3}. \end{aligned} \tag{4.7}$$

$$\begin{aligned} X_{uw} &= u, \\ Y_{uw} &= (2w - u)/\sqrt{3}. \end{aligned} \tag{4.8}$$

$$\begin{aligned} X_{vw} &= w + v, \\ Y_{vw} &= (w - v)/\sqrt{3}. \end{aligned} \tag{4.9}$$

Having located the event in XY plane, we can determine its location on the Z axis (or time t axis) by using the following constraint,

$$t = \frac{1}{2}(x_1 + x_2 - T_{sum}^x), \tag{4.10}$$

Where t is the arrival time of the atom on the detector and T_{sum}^x is the total propagation time along the x wire winding. One can similarly use y_1, y_2 or z_1, z_2 to find t . As the atoms free fall in the Z direction, the Z coordinate is given by $Z = -gt^2/2$. The (X, Y, t) position of the atoms thus obtained reflects the initial in-trap momentum-space distribution of the atomic cloud in the far-field. This allows for empirical measurement of various orders of momentum space correlation functions. In our case, we use the (X, Y, t) information to compute the second-order correlation function by histogramming the pair separations, for example by using the method as discussed in section 3.3.

4.3.4 Data Acquisition and Processing

In this section we take a short digression to discuss how raw pulses exiting the DLD wires are converted into the location information of the particles. The hardware following the DLD records the arrival times of the pulses arriving at the 6 ends of the 3 DLD wires. The small analogue pulse at the end of the DLD is converted to a digital pulse to record its arrival time (See Fig 4.14b, where an analogue pulse in top-yellow inset is converted to a digital pulse, as shown by a yellow pulse in the bottom). The digital pulse is then binned into 25ps time bins and written to a file with channel number vs time information. We have written a python script that matches signals from each of the 6 channels (namely x_1, x_2, y_1, y_2, z_1 and z_2) of the DLD, grouping them into an event (details in the next section). Lastly, by accounting for the hexagonal geometry of the DLD wire windings and the time required by the pulse to traverse the entire length of a wire, the event is assigned a position and time.

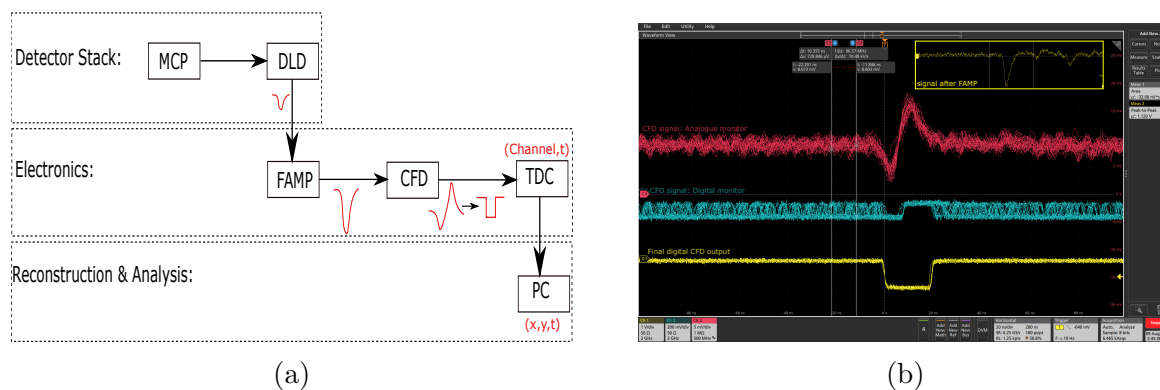


Figure 4.14: (a) Flowchart showing the pulse shape after each processing stage. (b) Oscilloscope trace showing the analogue pulse from FAMP (inset top-right) being converted to a digital pulse (bottom, yellow) by the CFD.

The auxiliary electronics like a fast-signal amplifier (FAMP), a constant fraction discriminator (CFD) and a time to digital converter(TDC) help in converting the raw pulse from DLD into channel number vs time data (4.14a). The FAMP or fast signal amplifier amplifies the fast (pulse duration $\sim 20ns$) and weak ($< 2mV$) analogue pulses to a measurable value of about 20mV. The CFD converts the amplified analogue pulse into a digital pulse which can be timed (Fig 4.14b). The pulses arriving at the same time from the FAMP, usually have variable amplitudes which can result in an error in estimating their time of arrival, as is the case with leading-edge discriminators that record the time at which a pulse attains certain specified slope (Fig 4.15b). However, the CFD circumvents this problem by inverting a fraction of the original pulse and adding it to the original pulse with a delay (Fig 4.15a). This results in an oscillatory pulse waveform (shown as the end product in Fig 4.15a) whose zero crossing value can be used as an accurate time measurement (as shown in Fig 4.15b). Hence, the CFD uses this timing information to output a digital pulse with the appropriate arrival time.

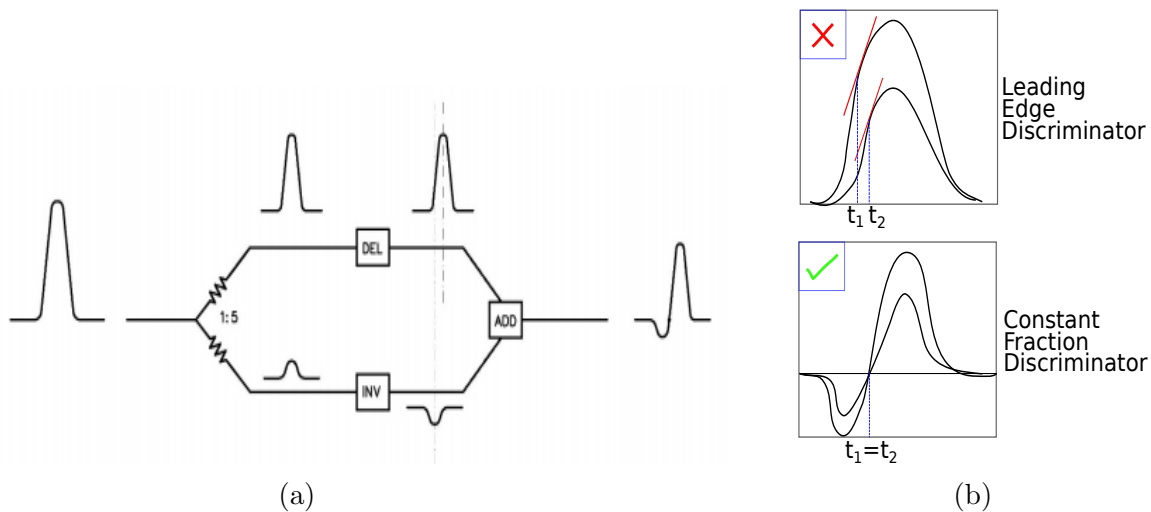


Figure 4.15: (a) Modification of analogue pulse to create a zero point crossing (along Y axis)[28]. (b) Pulses of variable height timed by leading edge (top) vs constant fraction discriminator (bottom).

The TDC then records these digital pulses by binning them into 25ps bins corresponding to the channel number (1-6) on which the pulse had arrived. The channel number vs time information is used by the PC to reconstruct events and write their position (X, Y) and time (t) of hitting the detector surface (details in the next section).

Event Reconstruction Algorithm

To obtain the (X, Y, t) coordinates of particles from the channel number vs time data output by the TDC, one needs to match the different pulses on the 6 different channels and group them into a single event (of a particle hitting the detector). It is usually the case that we get a pulse train of closely occurring events instead of single widely spaced pulses, and sometimes we may miss a pulse on one or more channels. Furthermore, we can have multi-hits within a narrow window of time which are difficult to resolve into separate events (In our case, we discard the multi-hits). Hence, to accurately reconstruct pulses into events, one needs to systematically scan through the pulses on the 6 channels and check for specific conditions for the pulses to be grouped into an event.

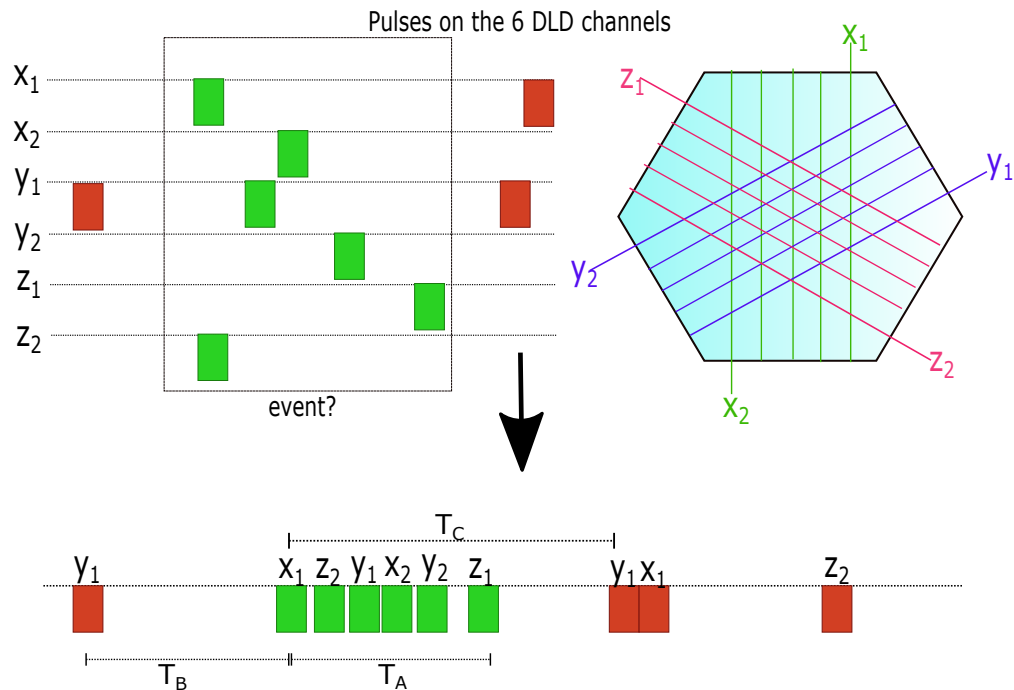


Figure 4.16: Grouping a set of 6 unique pulses from the ends of DLD (green) into an event by checking for certain conditions as mentioned below. The red pulses are assumed to belong to the neighbouring event while considering the green pulses as a candidate for an event.

To reconstruct the events we implement an algorithm to check for the following conditions (refer to Fig 4.16):

1. Loop through all the pulses in the channel number vs time data-set and select 6 consecutive pulses in time (say the green pulses in Fig 4.16) to check whether they belong

to the same event.

2. Check whether the group of 6 selected pulses consist of pulses from all the 6 unique channels (x_1, x_2, y_1, y_2, z_1 and z_2) and that they lie within a time window of T_{sum} from each other, that is, $T_A < T_{sum}$. The threshold is chosen to be T_{sum} as it's the maximum time that a pulse can take to arrive at the end of a DLD winding.
3. Check that this group is well separated in time from its neighbouring pulses to ensure that it doesn't contain a pulse that intersects with the neighbouring group (or event). This is implemented by checking the conditions $T_B > T_{sum}$ for comparison with the previous event and $T_C > T_{sum} + T_{dead}$ for comparison with the succeeding event, where $T_{dead} = 25ns$ is the dead time of the detector.

After reconstructing the events, one needs to convert the arrival time information into (X, Y, t) following the scheme discussed in section 4.3.3.

Note that for the reconstruction we have assumed that pulses from all 6 channels are present for the events. However, by making this assumption, we are ignoring events which have missing pulses on one or more channels. This is where the redundant information carried by the Hexanode delay line detector comes to the rescue, which allows one to reconstruct events with up to 3 out of 6 missing channels. This can be done by using the fact that the arrival time can be written in 3 different ways,

$$t = \frac{1}{2}(x_1 + x_2 - T_{sum}^x) = \frac{1}{2}(y_1 + y_2 - T_{sum}^y) = \frac{1}{2}(z_1 + z_2 - T_{sum}^z) \quad (4.11)$$

As these are 3 equations with up to 3 unknowns (timings of the missing pulses), we can figure out the value for the missing channel(s). For instance, in the case when one of the channel is missing (say x_1), we can salvage it by using the above equation in the following possible ways,

$$\begin{aligned} x_1 &= y_1 + y_2 - x_2 - T_{sum}^y + T_{sum}^x, \\ x_1 &= z_1 + z_2 - x_2 - T_{sum}^z + T_{sum}^x. \end{aligned} \quad (4.12)$$

Note that the redundant information reconstruction as discussed above was not tested or implemented in our system, due to time constraint, but is a next planned step for the detector.

4.3.5 Results: Reconstruction of DLD signals

To calculate a correlation function, one needs to have the (X, Y, t) coordinates of the atoms in the cloud as they hit the detector. As discussed in section 4.3.3, the signal arriving at the DLD from the MCP can be resolved spatially to give the (X, Y, t) coordinates of the atoms using the event reconstruction algorithm (section 4.3.4). We reconstruct the 3D profile for atoms released from the optical dipole trap (corresponding to the rightmost peak in the MCP trace 4.11) with and without evaporative cooling as summarised in Fig 4.17 and Fig 4.18 respectively. These figures contain 4 different subplots, namely, X-t, Y-t and X-Y histogram along with the full 3D XYt profile. The color-bar represents the number of atoms in the histogram bins.

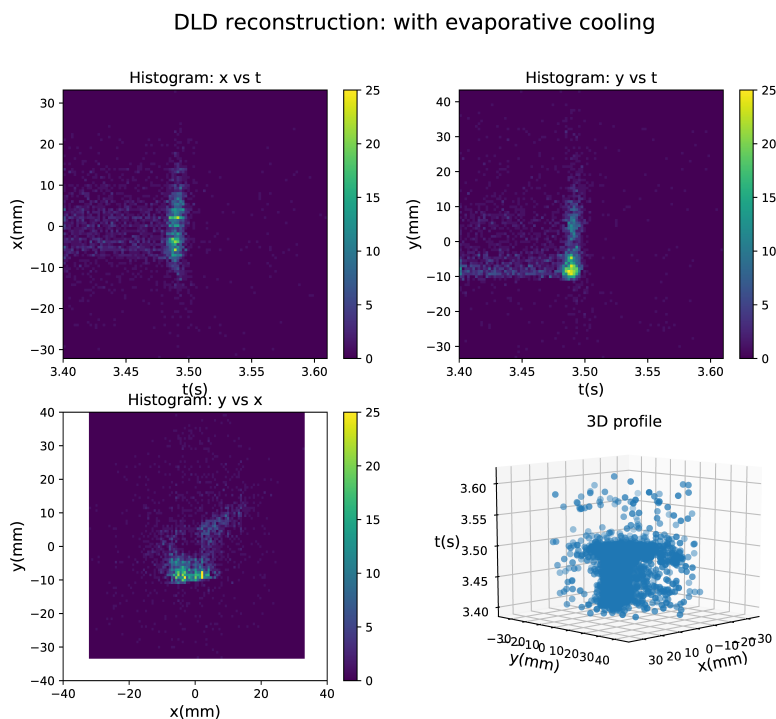


Figure 4.17: DLD reconstruction of atoms released from optical dipole trap with evaporative cooling. The images show the bi-modal distribution (close to $t=3.5$ s) with the BEC found at the high density region, accompanied by a narrow thermal tail around it.

We can observe that the X-t and Y-t histograms fall in a narrow time window for the cloud with evaporative cooling (Fig 4.17) than without the cooling (Fig 4.18). This is because cooling reduces the spread in velocities for the thermal component which is reflected in the

DLD reconstruction: without evaporative cooling

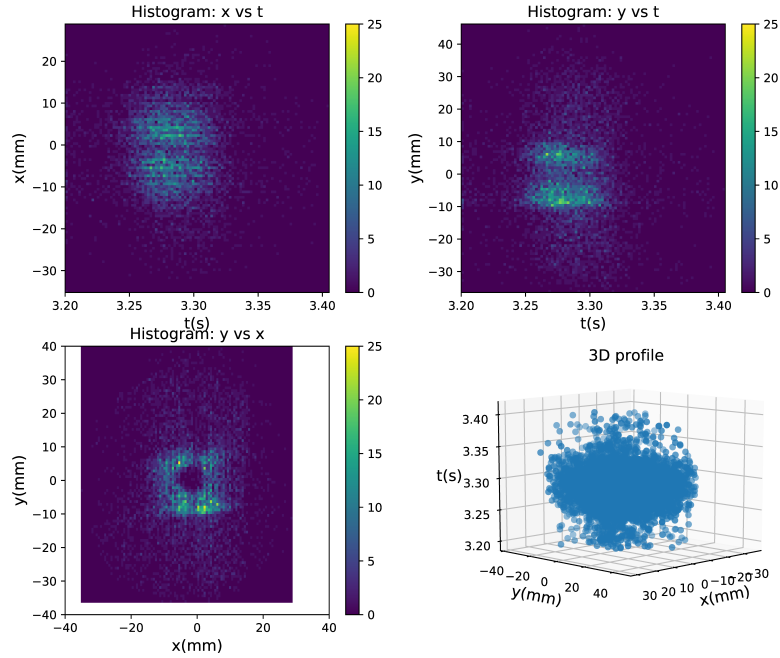


Figure 4.18: DLD reconstruction of atoms released from optical dipole trap without evaporative cooling. As the BEC fraction is reduced compared to Fig 4.17, more atoms now occupy the (broad) thermal part as seen in this figure.

temporal histograms. Furthermore, even the X-Y spatial widths of the cloud are narrower in the case with evaporative cooling due to the same reason as discussed above. One can notice that there seems to be a hole (lack of data points) around (0,0) in the X-Y histograms in both the figures. This could possibly be due detector saturation. Furthermore, the paper[26] shows the occurrence of a similar hole which it attributes to the electronic dead time of the detector of $\sim 10ns$, however the dead time is a single channel effect and we haven't observed any time delay across channels that could result in such a hole. Another point of concern is that we get a horizontal streak pattern close to $X=0$ in the X-t histograms and $Y=0$ in the Y-t histograms that suggest a lack of data on the streak line (clearer in Fig 4.18). Having this hole and the streak in the data poses a problem for calculation of correlation function, as some of the correlated data is lost. Apart from these issues, there is another major problem of inconsistent reconstructions (discussed in section 4.3.5) that limits our ability to calculate the correlation function using the above reconstructed 3D profile.

Calibrating the DLD parameters

There are three possible ways to reconstruct the positions of the particles, namely by using a pair of wires uv, uw or vw (see Eq 4.7, 4.8, 4.9). However, we observe that locations of particles obtained from the 3 reconstructions are not consistent with each other, that is, for a given particle, we obtain 3 different locations following the 3 reconstruction schemes. This can be seen in Fig 4.19b where we show a sample of 10 reconstructed triplets for a given data-set. From Fig 4.19b, notice that the 3 reconstructions are farther away from each other for some points compared to others (for instance, the top half compared to the bottom). Fig 4.19a shows the reconstructed points stacked over the MCP area of 80mm diameter.

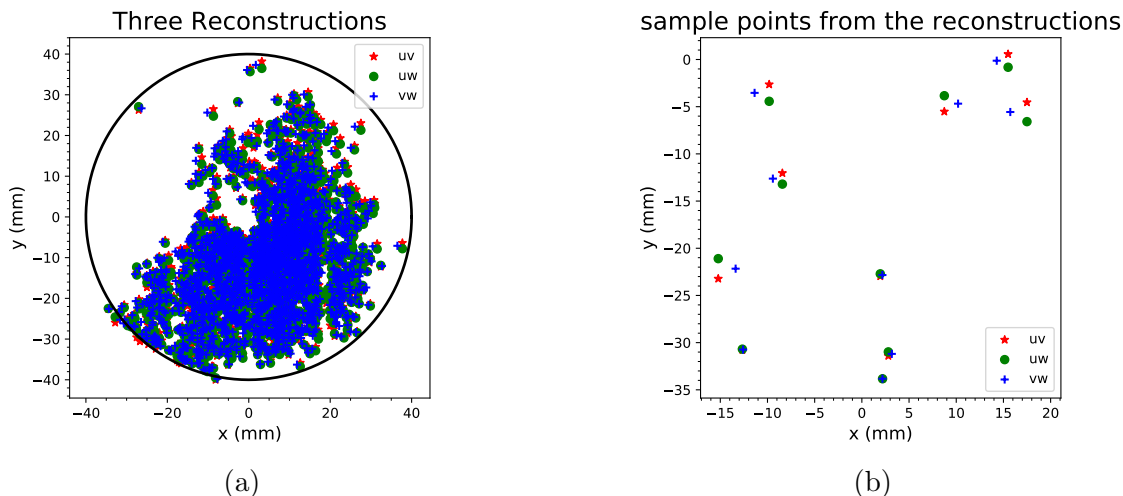


Figure 4.19: (a) The three reconstructions over MCP area (black circle). (b) 10 sample points from the three reconstructions.

Hence in an attempt to get the three reconstructions to agree (by bringing them as close as possible), we try to optimize the DLD parameters such as velocities (v_x, v_y, v_z) along the 3 wires and the relative offset (o) in one of the wires (see Eq 4.6). For the optimization, we define a cost function which is directly proportional to the distance between the 3 reconstructions, which we minimize with respect to the above mentioned free parameters. Furthermore, in order to prevent all the points from collapsing onto the origin (0,0), which may happen if the fit returns 0 velocities, we also penalize the cost function by dividing by the average distance of the 3 reconstructions from the origin. We measure the success of the optimization by the fraction of reconstructed triplets that lie within 1mm from their average position. Even after running the optimization routine, we are only able to get about 60-70%

of the triplets to lie within 1mm radius of each other (Fig 4.20a)

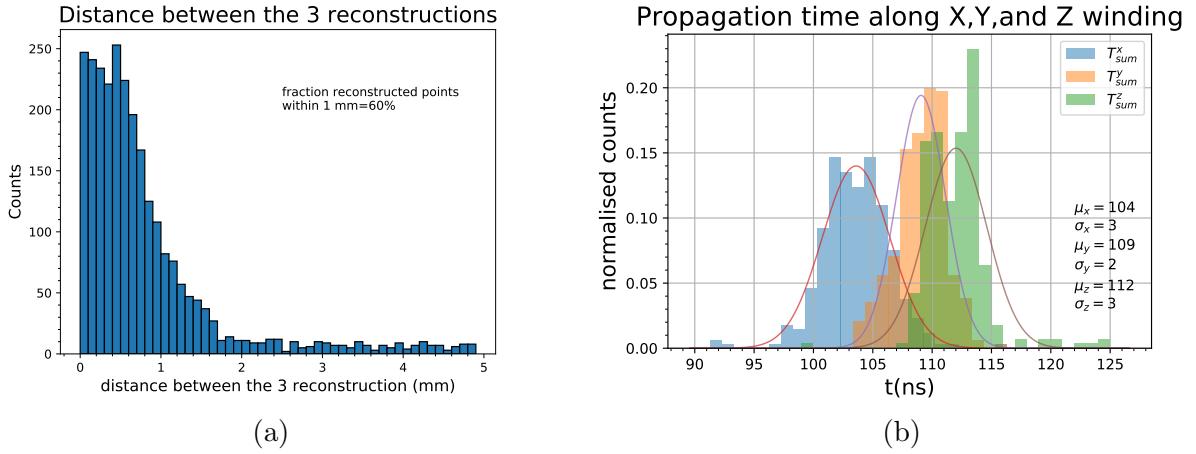


Figure 4.20: (a) Histogram showing the distribution of distances among the 3 reconstructions. (b) Estimating T_{sum} for each of the 3 wires by histogramming T_{sum}^i

Furthermore, as an alternate scheme to determine the velocities of propagation perpendicular to the 3 wires, we histogram the time sums $x_1 + x_2$, $y_1 + y_2$ and $z_1 + z_2$ to determine the propagation time, T_{sum} for each wire (see Eq 4.11, section 4.3.3 for definitions). The following Fig 4.20b shows a plot for $T_{sum}^i = r_1^i + r_2^i - 2t$, where $i = x, y, z$ and t is the time of arrival of the particle on the MCP. From this plot, we obtain the values of T_{sum} as summarised in the plot, which is $\sim 110ns$.

Furthermore, while watching the real-time pulses on each of the 6 ends of DLD, we observed that the pair of channels (y_1, z_2) and (y_2, z_1) had an artefact of correlated signals. That is, if the channels were independent of each other, then given a pulse on say y_1 at $t = t_0$, a pulse on z_2 could occur anywhere between $t_0 \pm T_{sum}$. However, we observe that the signal on z_2 occurs within $\sim t_0 \pm T_{sum}/2$ and hence doesn't span its whole range, similar is the case for (y_2, z_1) pair. This could be a possible cause for the disagreement between the 3 reconstructions as they use a different combination of u, v and w , which are now dependent on each other. In order to compute the correlation function for a cloud with a typical correlation length of $100\mu m$, the 3 reconstructions should agree at least within this distance from each other. Therefore, we cannot measure correlation functions until we can fix this issue. Due to time constraints, this could not be finished before the end of this project.

Chapter 5

Conclusion

In this thesis, we have achieved three broad outcomes, as presented below. Firstly, we managed to cool the He* atoms to degeneracy to obtain a Bose-Einstein condensate. For this purpose, we were required to optimise the cooling sequence focusing on in-trap cooling in the magnetic trap and evaporative cooling in the optical dipole trap. Secondly, we could simulate the 2nd order correlation function for a gas of thermal bosons. This was based on a simplistic modelling of pair correlations instead of sampling from the full and complicated many-body wavefunction for the bosons in a harmonic trap. However, this simplified approach was shown to be consistent with the analytical theory and the experimental results.

Lastly, we managed to set up the electronic detection system comprising the microchannel plates and the delay line detector which is useful for time of flight measurement for the atomic cloud dropped from a trap and to measure the correlation functions associated with the atomic cloud. Although due to the technical difficulties as highlighted in section 4.3.5, and time constraints to fix those, we could not actually measure the correlation function.

The future plan for the experiment is to troubleshoot the technical difficulties such as the artefact of inconsistent reconstruction, the hole and streak pattern in the reconstructed images. Having resolved these issues, the correlation function for a thermal gas of atoms and BEC can be measured and compared. Furthermore, interesting experiments such as observing the rate of decay of coherence during a dimensional crossover achieved by switching off one of the beams from the crossed optical dipole trap can be observed. This experiment is similar to an experiment[25], where the rate of buildup of coherence is studied while

crossing a Mott insulator to a superfluid phase transition. Furthermore, a long term plan for the lab is to set up the optical lattice, that is, a standing wave of light created by interference of two counter-propagating laser beams. The optical lattice would allow us to simulate prototypical condensed matter Hamiltonians with tunable parameters such as the Bose-Hubbard Hamiltonian, allowing us to perform experiments similar to the one described above[25].

Lastly, for the numerical simulation of correlation functions, it would be interesting to work out the details of how 3^{rd} and higher order correlation functions could be incorporated into the simulation. Including the higher order correlation functions should provide a more accurate picture of the many-body interaction statistics.

Appendix A

Monte-Carlo Rejection Sampling

Monte-Carlo Rejection (MCR) Sampling is a useful method for sampling from an arbitrary probability distribution $P(x)$ using a random number generator. While sampling from a 3D distribution, MCR has an advantage over the traditional inverse sampling method which requires one to know the analytical form for the inverse cumulative distribution function for the full and marginal probability distribution functions. Moreover, being a stochastic method, it provides a major speedup for the run-time.

As a simple example consider that one needs to sample from a Gaussian distribution (need not be normalised) with the distribution function $P_1(x) = \exp(-x^2/8)$. To generate points that follow this distribution, these steps can be followed:

1. Generate a random number from uniform distribution, $x_1 \sim U[a, b]$ in the interval $[a, b]$ which roughly spans the region where the target distribution $P_1(x)$ is non-zero. In this example we choose $a = -4, b = 4$ which are both equal to 2 standard deviations of the Gaussian (see Fig A.1).
2. Generate another random number from uniform distribution, say $x_2 \sim U[0, c]$ where $c = \max(P_1(x))$. The probability that it lies under the target distribution is proportional to $P_1(x_1)$ at the point x_1 . So we accept the point x_2 as following the distribution if it satisfies the condition,

$$x_2 < P_1(x_1) \tag{A.1}$$

if it doesn't satisfy this condition, we reject x_2 , otherwise we accept this trial point x_2 .

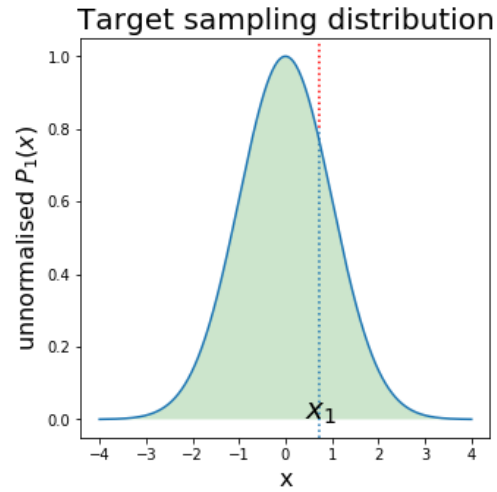


Figure A.1: The 1st point is sampled at x_1 . If the 2nd sampled point lies under the curve, that is, blue dotted line, it is accepted. If it lies on the red dotted line, it is rejected.

Bibliography

- [1] S. N. Bose. *Zeitschrift für Physik*. 26 (1): 178–181 (1924)
- [2] M. H. Anderson et al. *Observation of Bose-Einstein Condensation in a Dilute Atomic Vapor* *Science* Vol. 269, Issue 5221, pp. 198-201 (1995)
- [3] L. P. Pitaevskii, S. Stringari. *Bose-Einstein Condensation* Clarendon Press(2003)
- [4] C. Pethick, & H. Smith. *Bose–Einstein Condensation in Dilute Gases* Cambridge University Press. doi:10.1017/CBO9780511802850 (2008)
- [5] M. Fox. *Quantum Optics: An Introduction* OUP Oxford. ISBN 9780198566731 (2006)
- [6] H J. Metcalf, Peter van der Straten. *Laser Cooling and Trapping* Springer DOI: <https://doi.org/10.1007/978-1-4612-1470-0>
- [7] S. S. Hodgman, R. G. Dall, L. J. Byron, K. G. H. Baldwin, S. J. Buckman, and A. G. Truscott. *Metastable Helium: A New Determination of the Longest Atomic Excited-State Lifetime* *Phys. Rev. Lett.* 103, 053002(2009)
- [8] W. Vassen, C. Cohen-Tannoudji, M. Leduc, D. Boiron, C. I. Westbrook, A. G. Truscott, Ken Baldwin, G. Birkl, P. Cancio, and M. Trippenbach. *Cold and trapped metastable noble gases* *Rev. Mod. Phys.* 84, 175 (2012)
- [9] R. Brown and R. Twiss. *Correlation between Photons in two Coherent Beams of Light* *Nature* 177, 27–29 (1956)
- [10] U. Fano. *Quantum Theory of Interference Effects in the Mixing of Light from Phase-Independent Sources* *American Journal of Physics* 29, 539 (1961)
- [11] M. Yasuda and F. Shimizu *Observation of Two-Atom Correlation of an Ultracold Neon Atomic Beam* *Phys. Rev. Lett.* 77, 3090 (1996)
- [12] M. Schellekens, R. Hoppeler, A. Perrin, J. Viana Gomes, D. Boiron, A. Aspect, C. I. Westbrook *Hanbury Brown Twiss Effect for Ultracold Quantum Gases* *Science* Vol. 310, Issue 5748, pp. 648-651 (2005)

- [13] J. Viana Gomes, A. Perrin, M. Schellekens, D. Boiron, C. I. Westbrook, and M. Belsley. *Theory for a Hanbury Brown Twiss experiment with a ballistically expanding cloud of cold atoms* Phys. Rev. A 74, 053607 (2006)
- [14] S. S. Hodgman, R. I. Khakimov, R. J. Lewis-Swan, A. G. Truscott, and K. V. Kheruntsyan. *Solving the Quantum Many-Body Problem via Correlations Measured with a Momentum Microscope* Phys. Rev. Lett. 118, 240402 (2017)
- [15] R. J. Glauber *The Quantum Theory of Optical Coherence* Phys. Rev. 130, 2529 (1963)
- [16] S. S. Hodgman, R. G. Dall, A. G. Manning, K. G. H. Baldwin, A. G. Truscott. *Direct Measurement of Long-Range Third-Order Coherence in Bose-Einstein Condensates* Science Vol. 331, Issue 6020, pp. 1046-1049 (2011)
- [17] M. O. Scully, M. S. Zubairy. *Quantum Optics* Cambridge University Press (1997)
- [18] R. Loudon *The Quantum Theory of Light* OUP Oxford (2000)
- [19] T. Jelte, J. McNamara, W. Hogervorst et al. *Comparison of the Hanbury Brown–Twiss effect for bosons and fermions* Nature 445, 402–405 (2007).
- [20] R. Grimm et al. *Optical Dipole Traps for Neutral Atoms* Advances In Atomic, Molecular, and Optical Physics, Volume 42, 2000, Pages 95-170 (2000)
- [21] F. Shimizu, K. Shimizu, and H. Takuma *Double-slit interference with ultracold metastable neon atoms* Phys. Rev. A 46, R17(R) (1992)
- [22] R. G. Dall, A. G. Truscott. *Bose–Einstein condensation of metastable helium in a bi-planar quadrupole Ioffe configuration trap* Optics Communications, Volume 270, Issue 2 (2007)
- [23] I. Yavin, M. Weel, A. Andreyuk, and A. Kumarakrishnan. *A calculation of the time-of-flight distribution of trapped atoms* American Journal of Physics 70:2, 149-152 (2002)
- [24] S. Giorgini, L. P. Pitaevskii, S. Stringari. *Condensate fraction and critical temperature of a trapped interacting Bose gas.* Phys Rev A. (1996) R4633-R4636.
- [25] S. Braun, M. Friesdorf, S. Hodgman, M. Schreiber, J. Ronzheimer, A. Riera, M. del Rey, I. Bloch, J. Eisert, and U. Schneider. *Emergence Of Coherence And The Dynamics Of Quantum Phase Transitions* PNAS 112 (12) 3641-3646 (2015)
- [26] O. Jagutzki et al. *Multiple hit readout of a microchannel plate detector with a three-layer delay-line anode* IEEE Transactions on Nuclear Science, vol. 49, no. 5, pp. 2477-2483 (2002)
- [27] J. L. Wiza. *Microchannel plate detectors* Nuclear Instruments and Methods, Vol. 162, pages 587 to 601 (1979)
- [28] Roentdek CFD Manual <https://www.roentdek.com/manuals/CFD%20Manual.pdf>